

AD-A056 236

ARMY ARMAMENT RESEARCH AND DEVELOPMENT COMMAND ABERD--ETC F/G 20/8  
CHAMBERS FOR THE ELECTRODYNAMIC CONTAINMENT OF CHARGED AEROSOL --ETC(U)  
MAY 78 R H FRICKEL, R E SHAFFER

UNCLASSIFIED

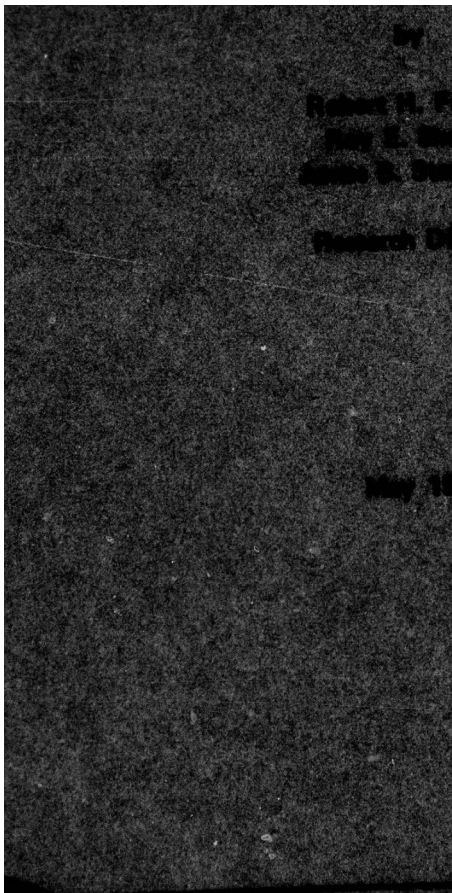
ARCSL-TR-77041

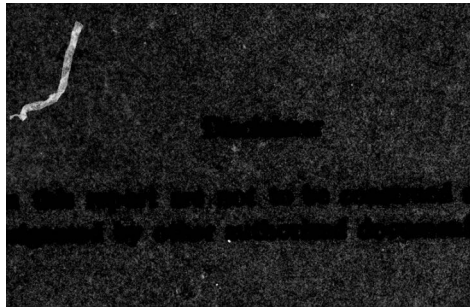
SBIE-AD-E410 033

NL

| OF |  
AD  
A056236







UNCLASSIFIED

SECURITY CLASSIFICATION OF THIS PAGE (When Data Entered)

REPORT DOCUMENTATION PAGE		READ INSTRUCTIONS BEFORE COMPLETING FORM
1. REPORT NUMBER 14 ARCSL-TR-77041	2. GOVT ACCESSION NO.	3. RECIPIENT'S CATALOG NUMBER
4. TITLE (and Subtitle) CHAMBERS FOR THE ELECTRODYNAMIC CONTAINMENT OF CHARGED AEROSOL PARTICLES.	5. TYPE OF REPORT & PERIOD COVERED Technical Report, June 1970-August 1971.	6. PERFORMING ORG. REPORT NUMBER
7. AUTHOR(s) Robert H. Frickel Roy E. Shaffer James B. Stamatoff	8. CONTRACT OR GRANT NUMBER(s) 16	
9. PERFORMING ORGANIZATION NAME AND ADDRESS Commander/Director, Chemical Systems Laboratory Attn: DRDAR-CLB-P Aberdeen Proving Ground, Maryland 21010	10. PROGRAM ELEMENT, PROJECT, TASK AREA & WORK UNIT NUMBERS Project 1B062116A081, Project 1T161101A91A	
11. CONTROLLING OFFICE NAME AND ADDRESS Commander/Director, Chemical Systems Laboratory Attn: DRDAR-CLJ-R Aberdeen Proving Ground, Maryland 21010	12. REPORT DATE May 1978	13. NUMBER OF PAGES 61 (12/6pp.)
14. MONITORING AGENCY NAME & ADDRESS (if different from Controlling Office)	15. SECURITY CLASS. (of this report) UNCLASSIFIED	15a. DECLASSIFICATION/DOWNGRADING SCHEDULE NA
16. DISTRIBUTION STATEMENT (of this Report) Approved for public release; distribution unlimited.		
17. DISTRIBUTION STATEMENT (of the abstract entered in Block 20, if different from Report)		
18. SUPPLEMENTARY NOTES		
19. KEY WORDS (Continue on reverse side if necessary and identify by block number) (U) Aerosols      Aerodynamic drag      Mathieu's equation Droplets      Electrodynamic containment      Bihemispheric electrodes Electrostatics      Evaporation of droplets      Bihyperboloidal electrodes Aerosol particles      Stroboscopic observations      Electroaerodynamic stability Charged droplets		
20. ABSTRACT (Continue on reverse side if necessary and identify by block number) (U) Chambers capable of the electrodynamic containment of electrostatically-charged 20- to 100-micron-diameter particles have been constructed, along with (a) a device for introducing a preselected particle into the chamber and (b) a system for measuring the charge, size, and motion of the particle. One of the chambers contains two hemispheres and a central ring; in the other, the two electrodes are hyperboloidal. The latter chamber incorporates additional provisions for the precise control of the temperature and composition of the gas in the chamber. Measurements of the particle motion agree with theoretical calculations.		

DDC  
RECEIVED  
JUL 17 1978  
B



## PREFACE

The work described in this report was authorized under Project 1B062116A081, Chemical Dissemination and Dispersion Technique. This work was started in June 1970 and completed in August 1971. The experimental data are recorded in notebook 8384.

The use of trade names in this report does not constitute an official endorsement or approval of the use of such commercial hardware or software. This report may not be cited for purposes of advertisement.

Reproduction of this document in whole or in part is prohibited except with permission of the Commander/Director, Chemical Systems Laboratory, Attn: DRDAR-CLJ-R, Aberdeen Proving Ground, Maryland 21010; however, Defense Documentation Center and the National Technical Information Service are authorized to reproduce this document for US Government purposes.

## Acknowledgments

The authors wish to acknowledge the technical assistance of H.W. Eppes and Charles M. Townsley for their invaluable contribution to the experimental work, and of Thomas E. Brewster for his assistance in computation.

ACCS	
DATE	
BY	
DIST	
BY	
DIST	
Dist	
A	

78 06 13 042

## CONTENTS

	<u>Page</u>
I. INTRODUCTION . . . . .	5
II. DESCRIPTION OF ELECTRODE CHAMBERS AND ASSOCIATED APPARATUS . . . . .	6
A. The Bihemispheric Electrode Configuration . . . . .	6
B. The Bihyperboloidal Electrode Configuration . . . . .	8
1. General . . . . .	8
2. Electrical System . . . . .	11
3. Observation Systems . . . . .	11
4. Thermal System . . . . .	12
5. Atmospheric System . . . . .	12
6. Particle Insertion Device and Method . . . . .	12
III. MOTIONS AND OBSERVATIONS OF CHARGED AEROSOL PARTICLES . .	14
A. Solutions of the Equation of Motion . . . . .	14
B. Experimental Verifications . . . . .	33
1. Verification of the Instability Boundary Curve . . . . .	33
2. Rate of Instabilization and the $\omega/2$ Boundary . . . . .	37
3. Passing Through the First Instability Region . . . . .	37
4. Phase Angle . . . . .	38
5. Particle Discharge . . . . .	39
6. Charge Decay Due to Cosmic Ray Ionization . . . . .	39
LITERATURE CITED . . . . .	41
APPENDIXES	
A. Derivation of Coefficients . . . . .	43
B. List of Symbols . . . . .	55
DISTRIBUTION LIST . . . . .	59

## LIST OF FIGURES

<u>Figure</u>		<u>Page</u>
1	Bihemispheric Configuration With Ring in Zero-Potential Plane . . . . .	7
2	Circuitry for Bihemispheric Configuration . . . . .	8
3	Chamber for Bihyperboloidal Configuration . . . . .	9
4	Cross-Section of Bihyperboloidal Configuration . . . . .	10
5	Circuitry for Bihyperboloidal Chamber . . . . .	10
6	Aerosol Particle Insertion Apparatus . . . . .	13
7	Instability Boundaries . . . . .	21
8	$E_1$ -Dependence of Instability Boundaries . . . . .	23
9	Phase Angle in Particle Oscillation . . . . .	24
10	Particle Distance Below Null Point, $V_{dc} = 0$ . . . . .	26
11	Lag Angle and Coincidence Point . . . . .	29
12	Amplitude of Vibration in Unstable Region . . . . .	30
13	A Suspended Glycerine Particle 80 $\mu\text{m}$ in Diameter . . . . .	33
14	Instability Boundary Curve . . . . .	36

## CHAMBERS FOR THE ELECTRODYNAMIC CONTAINMENT OF CHARGED AEROSOL PARTICLES

### I. INTRODUCTION.

Under proper conditions an electrically-charged aerosol particle can be contained at a point in space by an alternating electric field. This phenomenon may be used to make such a particle accessible for a variety of physical measurements. The obvious advantage of electrical suspension is to avoid artifacts required by mechanical suspension.

A positively-charged particle would remain at rest in stable equilibrium only at the point of minimum electrical potential within a potential well. However, Earnshaw's Theorem states that there cannot be an electrostatic potential well in free space; therefore, containment via electrostatic fields of a charged particle at a point in free space is impossible.

On the other hand, under the proper conditions an alternating electric field permits containment by producing on a charged particle a net time-averaged force directed toward a single point in space. The physical basis underlying this phenomenon may be explained by visualizing an electrically-charged particle oscillating in an alternating electric field. If this field is uniform (as between two flat, parallel, conducting plates), the charged particle oscillates at the driving frequency of the ac voltage, and the net (time-averaged) force is zero. If, however, an ac voltage is applied to an electrode with an arbitrarily curved geometric shape, a nonuniform electric field results, and an oscillating charged particle experiences net (time-averaged) forces in the directions of decreasing magnitude of instantaneous field strength. A charged particle can be contained within a small region of space by an alternating voltage on an electrode configuration whose electric field has a constant null point, e.g., on a ring electrode. The net (time-averaged) force toward the null point is used to counteract gravitational or other constant forces.

H. Strauble,<sup>1,2</sup> using a single-ring electrode connected to a high-voltage, low-frequency (50-hertz) source, succeeded in suspending electrically charged aerosol droplets with diameters between 30 and 100  $\mu\text{m}$ . R. F. Wuerker *et al.*<sup>3</sup> were able to contain small, electrically charged, metallic spheres in an evacuated chamber using hyperbolic electrodes and gave a brief theoretical discussion on the general motion of the contained particles. A. Muller<sup>4</sup> gave a more detailed theoretical treatment. For more recent applications of the same principles, the reader is referred to the work of K. S. Fansler *et al.*,<sup>5</sup> J. W. Schweizer and D. N. Hanson,<sup>6</sup> S. Ataman and D. N. Hanson,<sup>7</sup> and T. G. Owe Berg and T. A. Gaukler.<sup>8</sup>

Our primary objective was to determine the best electrode design for, and the usefulness of, the phenomenon of electrodynamic containment as an aid in basic studies of aerosol particles. To achieve this objective, theoretical calculations for idealized geometries were compared to experimental measurements for two electrode configurations.

For the purpose of computation it was assumed that the electric field varied linearly with distance in each direction from the null point, the vector proportionality constant being a function of direction; this assumption resulted in a linear differential equation of motion readily transposable into a modified Mathieu equation. The numerical calculations were performed using standard methods.



Two electrode configurations were chosen for the experimental work. A bihyperboloidal electrode configuration had the advantages of producing a radially linear electric field strength while completely enclosing the suspended particle. The chamber with the bihyperboloidal configuration made possible accurate verifications of the theoretical results. It was further equipped to operate under widely varying internal ambient conditions. As a result, this system has become a sophisticated tool for use in aerosol research. The second configuration consisted of a ring electrode and two hemispheric electrodes. Although its resulting field strength is only approximately radially linear, the simplicity of construction of this system was appropriate for initiating the work. Both configurations are described in detail in the next sections.

## II. DESCRIPTION OF ELECTRODE CHAMBERS AND ASSOCIATED APPARATUS.

The bihemispheric system, the bihyperboloidal system, the associated circuitry, and the apparatus for inserting charged particles are described in the following sections.

### A. The Bihemispheric Electrode Configuration.

Figures 1 and 2 show the apparatus for this case. Figure 1 is a photograph of the polystyrene and wood chamber. The brass ring electrode was connected to the ac high-voltage power supply through a voltage-dividing circuit that supplied the necessary voltage to the ring (49.4% of the ac voltage on the hemispheres) to insure an approximately linear field strength around the null point. Removable microscope slides, used as illumination and observation windows, allowed introduction of the aerosol particles. The ring also had a small arc removed to allow access of the particle-entry track to the interior of the chamber.

Figure 2 shows the schematic diagram of the electrical circuitry for the bihemispheric configuration. The variable ac voltage unit could be replaced with a variable-frequency device for obtaining driving frequencies other than 60 hertz. The dc voltage supply was designed to apply equal, opposite polarity voltages to the two hemispherical electrodes, leaving the ring plane at zero potential; the static field could then be calculated as that of the idealized geometry. The continuously variable dc power supply was capable of placing a maximum potential difference of 200 volts between the hemispheres.

One source of particle illumination was a strobe light positioned behind the chamber and facing the observer. When the strobe light was flashing at the same rate as the ac driving frequency, a single sharp image of the particle was visible through the microscope. With this type of illumination particle-size measurements could be made using a micrometer Filar eyepiece in the microscope.

An alternative light source consisted of a strip filament lamp with a vertical beam focused on a point in the vicinity of the null point from below the axis of the system. With this device, the moving particle could be viewed as a short white line against a much darker background.

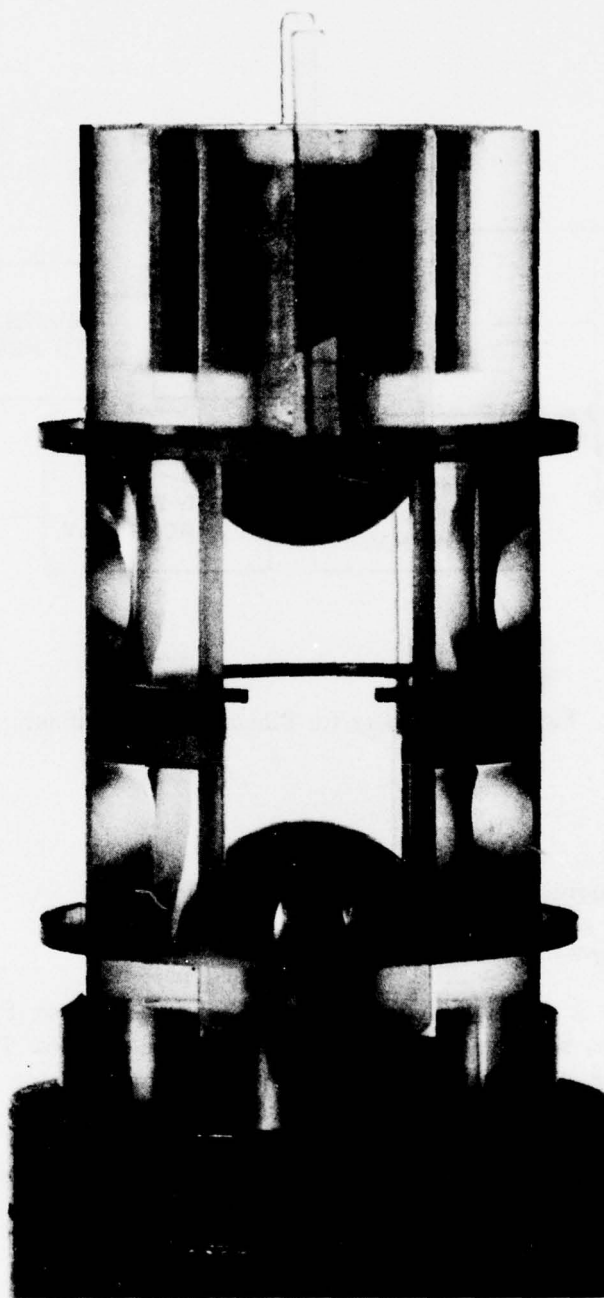


Figure 1. Bihemispheric Configuration With Ring in Zero-Potential Plant

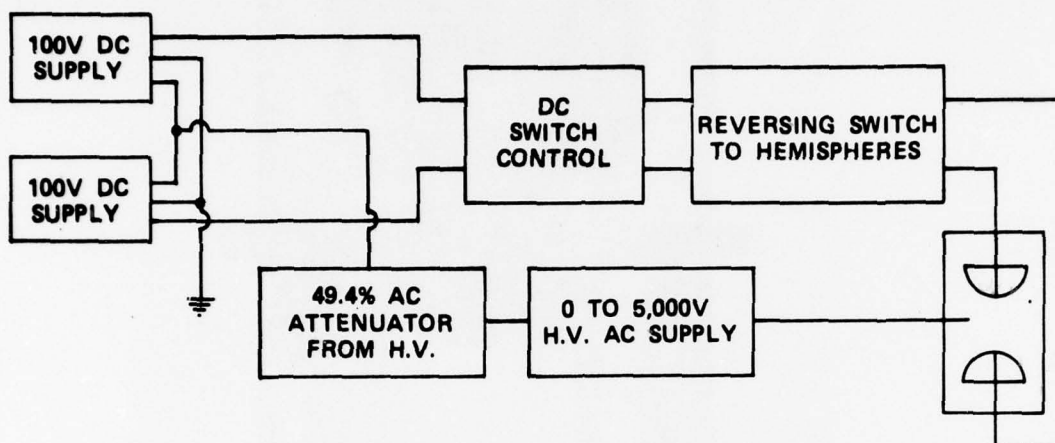


Figure 2. Circuitry for Bihemispheric Configuration

## B. The Bihyperboloidal Electrode Configuration.

### 1. General.

Figures 3, 4, and 5 depict the apparatus for this case. Figure 3 is a photograph of the Teflon chamber, showing the chrome-plated, brass electrodes. The chamber was thermally insulated by placing it entirely inside a cube of styrofoam. Figure 4 is a cross-section of the chamber.

To produce the desired electric field, the electrodes must be surfaces described by the equation

$$2z^2 - r^2 = C_{\pm}$$

where  $z$  and  $r$  are shown in figure 4 and  $C_{\pm}$  are constants, a positive constant for the two-sheet hyperboloid forming the top and bottom of the chamber, and a negative constant for the one-sheet hyperboloid forming the sides of the chamber.

These electrodes produce an electric field strength that is zero at the origin and has the described linearity, provided that the two sheets are at the same potential, as shown in section III.

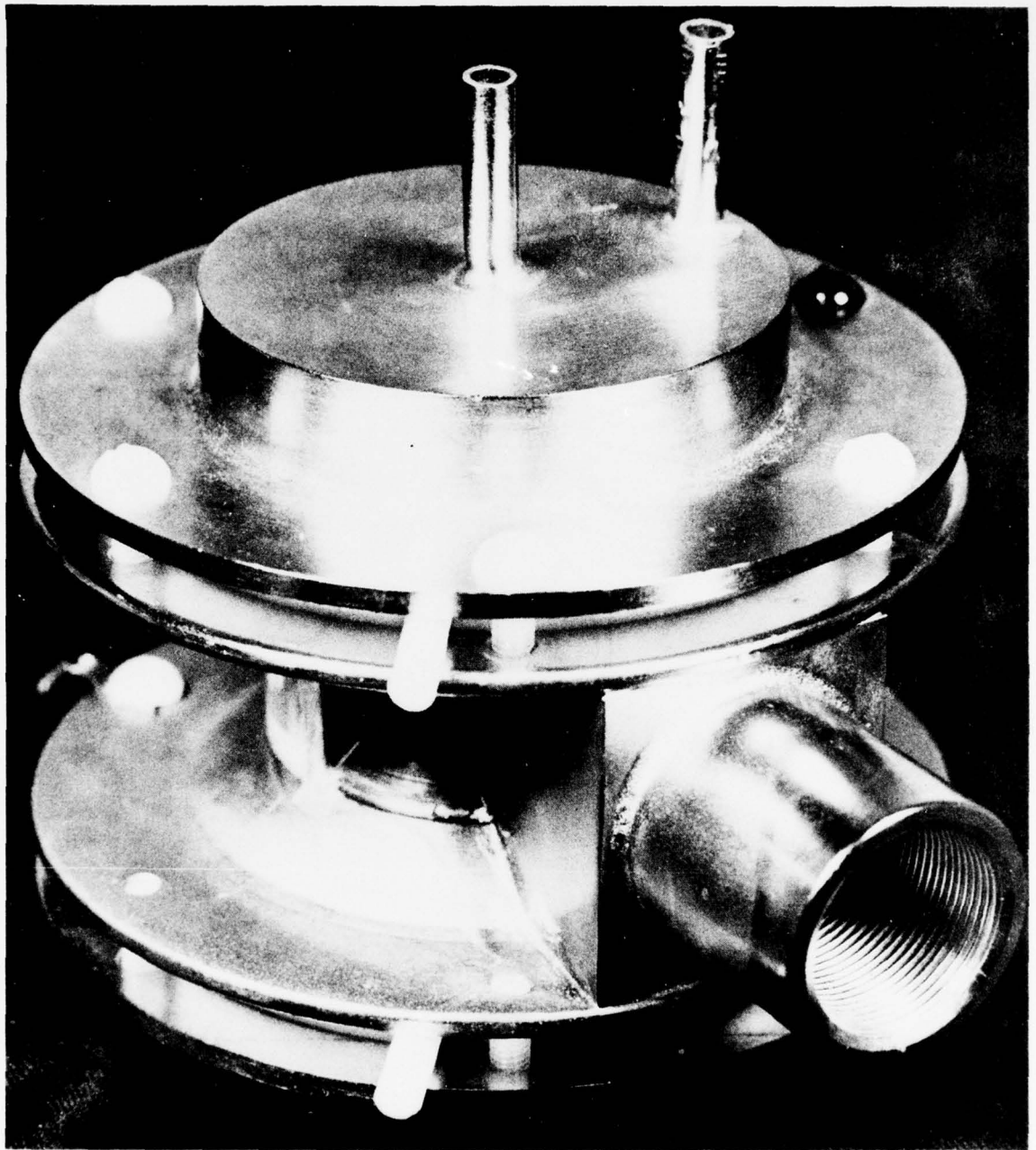


Figure 3. Chamber for Bihyperboloidal Configuration



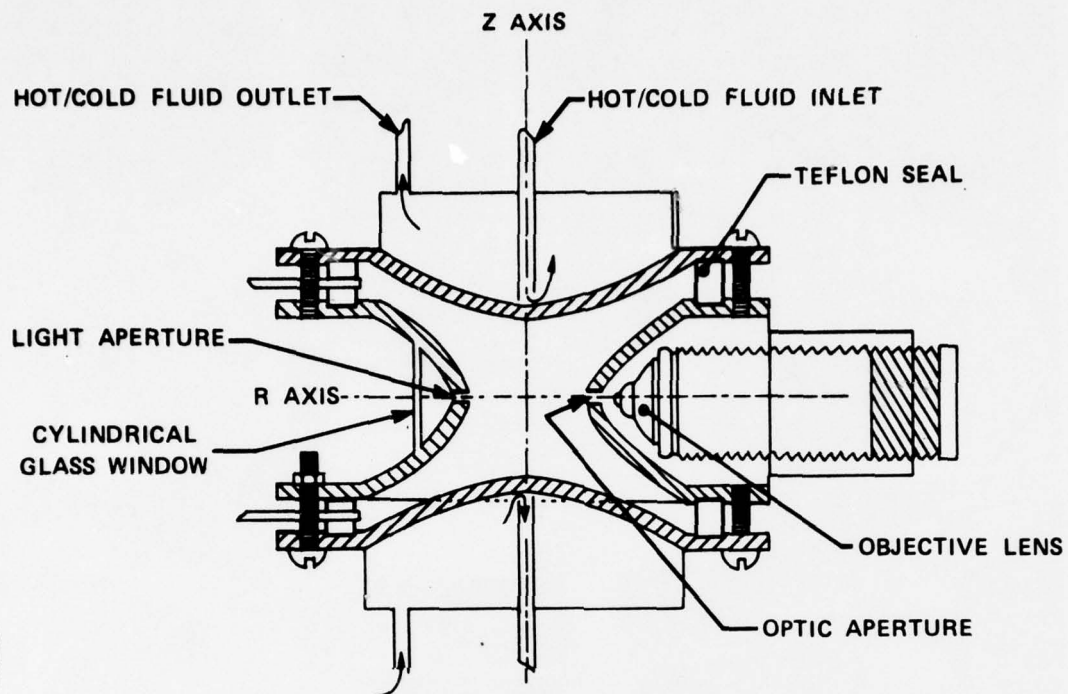


Figure 4. Cross-Section of Bihyperboloidal Configuration

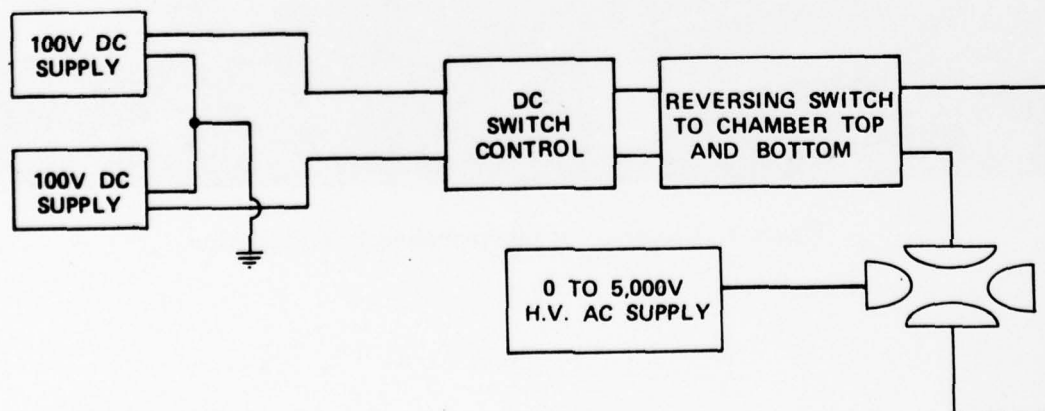


Figure 5. Circuitry for Bihyperboloidal Chamber

The top and bottom hyperboloidal sheets were separated from the central, single-sheet hyperboloid by two horizontal Teflon rings and could be fastened rigidly to the central hyperboloid with a set of six plastic screws and nuts. In practice, only the bottom sheet was fastened; the top sheet simply rested in place for easy removal.

Two collinear holes, 1/8 inch in diameter, were drilled diametrically opposite each other at the narrowest portion of the electrode. In viewing the suspended particles, one hole, sealed from the outside by a cylindrical glass window, formed an illumination port; the second hole, a viewing port, formed an optic aperture for the microscope objective lens.

## 2. Electrical System.

The circuitry used to produce the particle-suspending alternating electric field and the balancing constant electric field is shown in figure 5. The ac potential was impressed upon the one-sheet hyperboloidal conductor. The dc potential was impressed symmetrically on the top and bottom sheets of the two-sheet hyperboloidal electrode, above and below, respectively, the common ground with respect to which the ac potential oscillated.

The symmetry of the dc potential was maintained by a series of variable potentiometers for a range of potential differences up to 200 volts. A scaling switch permitted the most accurate use of the two synchronized helipot controls that controlled this voltage.

The ac supply, variable up to 4,000 volts, originated from a high-voltage transformer. The input to this transformer could be either from line voltage or from a Belman-Invar Invertron power amplifier connected to a variable oscillator. Because the study utilized a 60-hertz ac electric field, line voltage was acceptable as input.

A Kintel Model 301 standard dc voltage supply, a potentiometer, and precision resistance boxes were used to calibrate both ac and dc potentials. The voltages were monitored with a Honeywell model 1108 Visicorder and a Tektronix type 564 storage oscilloscope. The dc voltage could be determined to an accuracy of  $\pm 0.5$  volts, and the ac voltage to an accuracy of  $\pm 10$  volts.

## 3. Observation Systems.

The two modes of observing suspended particles were direct observation through a microscope eyepiece and photographic observation utilizing a 32-millimeter movie camera.

Lighting for both of these modes was provided by a General Radio type 1538-A stroboscope firing through the back-lighting port. The strobe frequency could be manually varied from 110 to 150,000 flashes per minute. Because the apparatus normally operated at 60 hertz, the stroboscope was automatically synchronized with the 60-hertz line voltage. A time-delay device permitted the observation of particles at any point in their 60-hertz vertical oscillations. A circuit that automatically doubled the stroboscope frequency to 120 hertz was also introduced to produce double images of the particles. With the proper time delay the separation of the two images of a particle would reach a maximum corresponding to the oscillation endpoints separation.

The particle image seen through the second port was formed using a Bausch and Lomb 32-mm focal length microscope objective lens with a numerical aperture of 0.10 in

conjunction with a Vickers-AEI image-splitting eyepiece mounted at the end of a 6-inch-long optical tube equipped with an adjustable iris. The optical apparatus, supported by a tripod, was physically independent of the chamber. When viewing the particle, the observer adjusted the eyepiece tube to touch the tube containing the objective lens, obtaining a focused image with a fixed magnification. The eyepiece could then be calibrated for measuring particle diameters. Its image-splitter consisted of a prism controlled by a ruled micrometer. By bringing the two split images into apparent contact, a diameter measurement could be made in the range 10 to 250  $\mu\text{m}$  with an accuracy of  $\pm 1 \mu\text{m}$ .

The 32-mm movie camera required a bright source of light flashing at a suitable frequency while the camera shutter was open. These requirements were met by use of a multiple timer, additional electronic circuitry, and a large capacitor attached to the stroboscope. The resulting film records of suspended particles were useful in analyzing the changes in shape and size of the particles.

#### 4. Thermal System.

The top and bottom sheets of the bihyperboloid electrode configuration contained reservoirs for liquid (see figure 4) that were used to control the temperature of the chamber. Once a given chamber temperature had been established, it was maintained by the insulating foam enclosure. Because measurements of the dc balancing voltage and the ac splitting voltage (see section III) were severely affected by thermally-induced convection currents, the observer had to wait for thermal equilibrium for 1/2 hour from the time liquid circulation ceased before taking measurements.

A small thermocouple, inserted through the lower Teflon ring and connected to the Honeywell Visicorder allowed the temperature of the interior of the chamber to be determined to within  $\pm 1^\circ\text{C}$ .

#### 5. Atmospheric System.

Ports in both the top and bottom Teflon rings were used to control the ambient atmosphere in the chamber. With appropriate equipment connected to these ports, the desired pressure and composition of the gas in the chamber could be established.

In the calibration experiments, very low ambient humidity was obtained by slowly circulating air first through phosphorus pentoxide and then through the chamber. This air circulation was stopped during measurements.

#### 6. Particle Insertion Device and Method.

Figure 6 is a photograph of the apparatus used to insert aerosol-sized particles into a chamber. This apparatus consisted of three 22-inch, parallel, metal rods. One rod was placed below the other two rods so that the cross-section formed a V-shaped track supported by a small, notched, plastic rectangle on one end and by a larger rectangular plastic shield on the other end. The top two rods, joined behind the plastic shield by a loop, were connected to the ac voltage source. The bottom rod was rounded. The open end of the track was placed in the chamber (in the case of the bihyperboloidal chamber, after removal of the upper sheet).

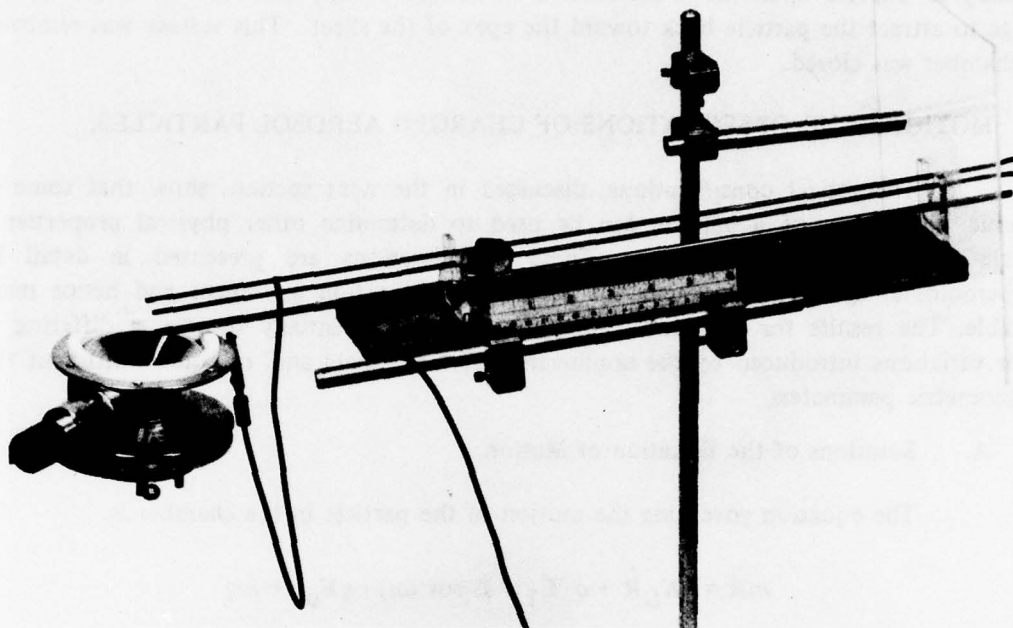


Figure 6. Aerosol Particle Insertion Apparatus

The liquid or dissolved solid to be studied was placed inside a glass capillary tube that was connected to a variable dc high-voltage source normally operating between 4,000 and 10,000 volts. A polydisperse spray of charged particles was then obtained by striking the capillary tube, causing it to vibrate.

These particles were allowed to fall through the loop connecting the two upper rods, where particles with appropriate charge and mass, depending on the voltage on the rods, were captured; the track was then tilted downwards toward the chamber to move the particles. All particles except the one selected for observation were removed from the track (or, if necessary, from the chamber) by means of plastic rods that attracted the unwanted particles either by induction or by virtue of being charged oppositely to the charge on the particles. Once the selected particle was in the chamber, the track was removed. In the case of the bihyperboloidal system, the upper sheet was then replaced.

It was found necessary to assist the initial capture of the particle in the chamber by impressing a dc voltage on the electrodes. In the case of the bihemispheric system, this was approximately a gravity-balancing voltage. In the case of the bihyperboloidal system, however, the ac field, distorted by the removal of the upper sheet, repelled the particle from the apex of the lower sheet, permitting it to slide down and out of the containing volume; it was therefore



necessary to impress upon the lower sheet a dc voltage of opposite sign to the gravity-balancing voltage to attract the particle back toward the apex of the sheet. This voltage was removed when the chamber was closed.

### III. MOTIONS AND OBSERVATIONS OF CHARGED AEROSOL PARTICLES.

Theoretical considerations, discussed in the next section, show that some electrodynamic parameters of a particle can be used to determine other physical properties of the particle such as charge and mass. These considerations are presented in detail for the bihyperboloidal system, for which the equations of motion are linear and hence reasonably tractable. The results for the bihemispheric system are essentially the same, differing only in minor variations introduced by the nonlinearity of the ac field and, of course, different values of the geometric parameters.

#### A. Solutions of the Equation of Motion.

The equation governing the motion of the particle in the chamber is

$$m\ddot{\mathbf{R}} = -K_D\dot{\mathbf{R}} + q(\mathbf{E}_1 + \mathbf{E} \cos \omega t) + q\mathbf{E}_{dc} + m\mathbf{g} \quad (1)$$

where

- $\mathbf{R}$  = position of the particle relative to null point
- $m$  = mass of the particle
- $q$  = charge on the particle (considered positive here)
- $K_D$  = coefficient describing aerodynamic drag force
- $\mathbf{E} \cos \omega t$  = the alternating part of null-point field
- $\mathbf{E}_1$  = constant part of null-point field
- $\omega$  = angular frequency of applied voltage
- $t$  = independent variable, time
- $\mathbf{E}_{dc}$  = static field between the upper and lower portions of the outer electrode where these parts are at different potentials
- $\mathbf{g}$  = acceleration due to gravity

NOTE: Dots indicate differentiation with respect to time.

For small values of the Reynolds number,  $Re (= \rho d |\dot{\mathbf{R}}| / \eta)$ ,  $K_D$  is given by

$$K_D = 3\pi\eta d \quad (\text{Stokes' Law})$$

where  $d$  is the particle diameter, and  $\eta$  and  $\rho$  are the viscosity and density of the air, respectively. For larger values of the Reynolds number a correction term must be added, as in the formula due to Oseen:

$$K_D = 3\pi\eta d(1 + \frac{3}{16}\text{Re})$$

Any cylindrically symmetric potential function in charge-free space can be written in the form

$$\Phi = \sum_{n=0}^{\infty} \bar{A}_n r_s^n P_n(\cos \theta_s)$$

where  $r_s$  and  $\theta_s$  are the radial and polar angle coordinates of a spherical coordinate system,  $P_n(\cos \theta_s)$  are Legendre polynomials, and the constant coefficients  $\bar{A}_n$  depend on the geometry of the field source.

If the potential is also symmetric about the plane  $\theta = \frac{\pi}{2}$ , as in the null-point fields considered here, the odd-term coefficients are all zero. If the series is now rewritten in cylindrical coordinates  $r, \theta, z$  the field becomes

$$\begin{aligned} \Phi = & A_0 + A_2(r^2 - 2z^2) + A_4(3r^4 - 24r^2z^2 + 8z^4) \\ & + A_6(5r^6 - 90r^4z^2 + 120r^2z^4 - 16z^6) + \dots \end{aligned} \quad (2)$$

where  $A_n$  are a new set of constant coefficients. In the case of the bihemispheric configuration, the potentials relative to a distant ground on the ring and on the spheres were adjusted so that  $A_4 = 0$ , leaving in the series (besides the quadratic term) only terms of sixth and higher powers, which are very small in the region around the origin. The potential is then approximated by

$$\Phi = A_0 + A_2(r^2 - 2z^2) \quad (3)$$

If the quartic and higher terms of equation 2 are dropped altogether, so that equation 3 is exact, the equipotentials are hyperboloids of revolution described by

$$r^2 - 2z^2 = \frac{\Phi - A_0}{A_2} \quad (4)$$

the right-hand side being constant on an equipotential. The electrodes in the bihyperboloidal configuration are described by

$$r^2 - 2z^2 = r_0^2 \quad (5)$$

$$r^2 - 2z^2 = -2z_0^2 \quad (6)$$

where  $r_0$  is the radius of the one-sheet hyperboloid and  $2z_0$  is the distance between the upper and lower sheets of the two-sheet hyperboloid. The values of  $A_0$  and  $A_2$  can be found by noting that the two-sheet hyperboloid is grounded ( $\Phi = 0$ ), and that the potential  $\Phi$  on the one-sheet hyperboloid is  $-V \cos \omega t$  (where  $V$  is the peak voltage), equating the right-hand sides of equations 4 and 5, and equating the right-hand sides of equations 4 and 6. When these values are substituted into equation 3, the expression for  $\Phi$  becomes

$$\Phi = \frac{V \cos \omega t}{r_0^2 + 2z_0^2} (2z^2 - r^2 - 2z_0^2)$$

on the electrodes and inside the chamber.

The electric field  $E_c$  is

$$E_c = -\nabla \Phi = \frac{4V \cos \omega t}{r_0^2 + 2z_0^2} \left( \frac{r}{2} \hat{r}_0 - z \hat{k} \right) \quad (7)$$

where  $r_0$  and  $\hat{k}$  are the radial and axial unit vectors, respectively. In the work covered by this report  $\hat{k}$  is directed upward. The choice of sign for the potential on the one-sheet hyperboloid is arbitrary. If the voltage on the one-sheet hyperboloid is biased with respect to ground, its potential is  $-V_1 - V \cos \omega t$  and

$$E_c = \frac{4(V_1 + V \cos \omega t)}{r_0^2 + 2z_0^2} \left( \frac{r}{2} \hat{r}_0 - z \hat{k} \right)$$

Note that

$$E_c = E_1 + E \cos \omega t$$

where  $E_1$  and  $E$  are defined in equation 1.

The quantity  $E_{dc}$  is the field produced by imposing a static potential difference between the two sheets of the two-sheet hyperboloid. The expression for the potential from this source contains only the odd terms of the Legendre polynomial expansion and the field in cylindrical coordinates is

$$E_{dc} = A_1 \hat{k} + [4A_3 z + A_5 (3r^2 - 4z^2)z + \dots] \hat{r}_0 \quad (8)$$

$$+ [A_3 (2r^2 - 3z^2) + 2A_5 (5z^2 - 3r^2)z + \dots] \hat{k}$$

In this investigation higher power terms are dropped and  $E_{dc}$  is approximated as

$$E_{dc} = A_1 \hat{k} = C_{dc} V_{dc} \hat{k} \quad (9)$$

where  $V_{dc}$  is the potential difference between the sheets ( $V_{dc} > 0$  if the lower sheet is at the higher potential) and  $C_{dc}$  is an experimentally determined geometric constant. Equation 9 is exact in two cases, to wit: (1) when  $V_{dc} = 0$  and the particle oscillates below the null point only under the influence of the null-point ac field and gravity, and (2) when the particle is balanced at the null point because

$$qE_{dc} + mg = 0$$

$r$  and  $z$  are then zero and the higher power terms of equation 8 vanish.

The principal situation of interest in this investigation for which equation 9 is not exact occurs when the particle is balanced at the null point but is oscillating about the null point because it is in an unstable region of the  $\kappa$ - $E$  chart (described later in this section).

The axis of symmetry of the apparatus is vertical so that

$$g = -g\hat{k}$$

To transform equation 1 into dimensionless form, let

$$\tau = \omega t \quad (10a)$$

$$\xi_1 = x/d \quad (10b)$$

$$\xi_2 = y/d \quad (10c)$$

$$\xi = z/d \quad (10d)$$

where  $x$ ,  $y$ , and  $z$  are the cartesian coordinates of  $R$ , and  $d$  is the particle diameter. Let equation 10 be substituted into equation 1 and the latter be divided by  $\omega^2$ . Then equation 1 written in terms of its components is

$$\xi'' + (\kappa + \kappa_1 u)\xi' + (E \cos \tau + E_1)\xi + h = 0 \quad (11)$$

$$\xi'' + (\kappa + \kappa_1 u)\xi' - \frac{1}{2}(E \cos \tau + E_1)\xi = 0 \quad (12)$$



where the primes denote differentiation with respect to  $\tau$ , and where

$$\kappa = \frac{18\eta}{\rho_s \omega d^2}$$

$$u = |R'|/d$$

$$E_1 = \frac{Cq}{\omega^2 m} V_1$$

$$E = \frac{Cq}{\omega^2 m} V$$

$$h = \frac{g}{\omega^2 d} - \frac{C_{dc} q}{\omega^2 dm} V_{dc}$$

$\xi$  represents  $\xi_1$  or  $\xi_2$ ,  $\rho_s$  is the density of the particle material, and  $C$  is the geometric constant relating the potential on the electrodes to the null-point field strength. From equation 7 it is easy to see that for hyperboloidal electrodes,

$$C = \frac{4}{r_0^2 + 2z_0^2}$$

Because  $r_0 = 1.25$  cm and  $z_0 = 1.75$  cm for the device described in this report,  $C = 5,203 \text{ m}^{-2}$ .

If the aerodynamic drag is described by Stokes' Law,

$$\kappa_1 = 0$$

If the drag is described by Oseen's Law,

$$\kappa_1 = \frac{27}{8} \frac{\rho}{\rho_s}$$

Now equations 11 and 12 are of essentially the same form; for reasons that will become clear later, equation 11 has more physical significance than equation 12, and the discussion will concentrate on equation 11 but is applicable to both. Solutions are first discussed for the case of Stokes' Law, and the effects of deviations from Stokes' Law are considered later. For Stokes' Law equation 11 is linear, viz.:

$$\xi'' + \kappa \xi' + (E \cos \tau + E_1) \xi + h = 0 \quad (13)$$

The solution of equation 13 has the form

$$\xi = A\xi_1(\tau) + B\xi_2(\tau) + p(\tau) \quad (14)$$

where  $\xi_1$  and  $\xi_2$  are independent solutions of the homogeneous equation

$$\xi'' + \kappa\xi' + (E \cos \tau + E_1)\xi = 0 \quad (15)$$

and

$$p(\tau) = \sum_{n=-\infty}^{\infty} a_n e^{in\tau} \quad (16)$$

The method of calculating the coefficients  $a_n$  is shown in appendix A. The coefficients  $a_n$  are proportional to  $h$  and vanish if  $h = 0$ . By means of the transformation

$$\tau = 2\bar{\tau} \quad (17a)$$

$$\xi = e^{-\kappa\bar{\tau}} \bar{\xi} \quad (17b)$$

equation 15 may be written as the Mathieu equation

$$\bar{\xi}'' + (\bar{a} - 2\bar{q} \cos 2\bar{\tau})\bar{\xi} = 0$$

where  $\bar{a}$  and  $\bar{q}$  are constants. Properties of  $\xi_1$  and  $\xi_2$  may then be discussed in terms of the well-known properties of solutions to the Mathieu equation. From this comparison (see appendix A) it is seen that the solutions  $\xi_1$  and  $\xi_2$  should be of the form

$$\xi_1 = e^{-\frac{1}{2}\kappa\tau} e^{\gamma\tau} P(-\tau) \quad (18a)$$

$$\xi_2 = e^{-\frac{1}{2}\kappa\tau} e^{-\gamma\tau} P(-\tau) \quad (18b)$$

where  $P(\tau)$  is a bounded periodic function with period  $2\pi$ , and  $\gamma$  can take one of the forms

$$\gamma = \alpha \quad (19a)$$

$$\gamma = \alpha + \frac{1}{2}i \quad (19b)$$

$$\gamma = \beta i \quad (19c)$$

where  $\alpha$  and  $\beta$  are real. It is evident that  $\alpha$  may be considered positive without loss of generality. The coefficients  $A$  and  $B$  of equation 14 can be calculated from the conditions at any particular value of  $\tau$ ; in general neither vanishes. Therefore  $\xi$  is stable (bounded for  $\tau > 0$ , where  $\tau = 0$  represented the initial situation) only if  $\xi_1$  and  $\xi_2$  are both stable, i.e.,

$$R(\gamma) - \frac{1}{2}\kappa < 0$$

$$-R(\gamma) - \frac{1}{2}\kappa < 0$$

whence

$$\frac{1}{2}\kappa > R(\gamma) - \frac{1}{2}\kappa$$

where  $R(\gamma)$  is the real part of  $\gamma$ . This condition is obviously satisfied for the case

$$\gamma = \beta i$$

and requires that  $\alpha \leq \kappa/2$  in equation 19. A method for calculating  $\gamma$  is shown in appendix A.

A chart showing the nature of  $\gamma$  as a function of  $\kappa$  and  $E$ , for  $E_1 = 0$ , is shown in figure 7. In the space defined by  $\kappa$  and  $E$  there is a series of regions where  $\alpha \neq 0$  that are separated by regions where  $\gamma = \beta i$ . In the former regions  $\gamma$  is alternately given by  $\gamma = \alpha$  and  $\gamma = \alpha + \frac{1}{2}i$ . It is evident that in regions where  $\gamma = \alpha$  the periodicity of  $\xi$  is  $2\pi$ , and that in regions where  $\gamma = \alpha + \frac{1}{2}i$ , the periodicity of  $\xi$  is  $4\pi$ ; in regions where  $\gamma = \beta i$  the function is in general not periodic. On the boundaries between  $\gamma = \beta i$  and  $\gamma = \alpha$ ,  $\alpha$  and  $\beta$  both vanish, so that  $\gamma = 0$ . On the boundaries between  $\gamma = \beta i$  and  $\gamma = \alpha + \frac{1}{2}i$  regions,  $\gamma = \frac{1}{2}i$ . In the interiors of the regions where  $\alpha \neq 0$  are regions where  $\alpha > \frac{1}{2}\kappa$ ; in these interior regions the solution  $\xi$  of equation 13 is not stable. The curves on which  $\alpha = \frac{1}{2}\kappa$  are the boundaries between regions of stable and unstable solutions of equation 13 and are designated as instability boundaries or quasi-instability boundaries in this report. Figure 7 shows the first such unstable region and part of a second.

In region  $R_0$  in figure 7,  $\gamma$  is real, but  $\alpha$  never exceeds  $\frac{1}{2}\kappa$ ; the function  $\xi$  is stable everywhere in  $R_0$  and there is no instability boundary. The periodicity of  $\xi$  in  $R_0$  is  $2\pi$ . In the region  $I_1$ ,  $\gamma = \beta i$ , and  $\xi$  is stable and nonperiodic. In regions  $R_{1,S}$  and  $R_{1,U}$ ,  $\gamma = \alpha + \frac{1}{2}i$ , and the period of  $\xi$  is  $4\pi$ . In  $R_{1,S}$ ,  $\alpha < \frac{1}{2}\kappa$ , and  $\xi$  is stable; in  $R_{1,U}$ ,  $\alpha > \frac{1}{2}\kappa$ , and  $\xi$  is unstable. The boundary between  $R_{1,S}$  and  $R_{1,U}$  is the first instability boundary. In the regions  $R_{2,S}$  and  $R_{2,U}$ ,  $\gamma = \alpha$ , and the period of  $\xi$  is  $2\pi$ . The second instability boundary separates  $R_{2,S}$ , where  $\alpha > \frac{1}{2}\kappa$ , and  $\xi$  is unstable. Between  $R_{1,S}$  and  $R_{2,S}$  lies the narrow region  $I_2$ , where  $\gamma = \beta i$ , and  $\xi$  is stable and nonperiodic. The quantity  $\nu$ , shown in figure 7 are curves of constant  $\nu$ , is given by

$$\nu = \alpha - \frac{1}{2}\kappa$$

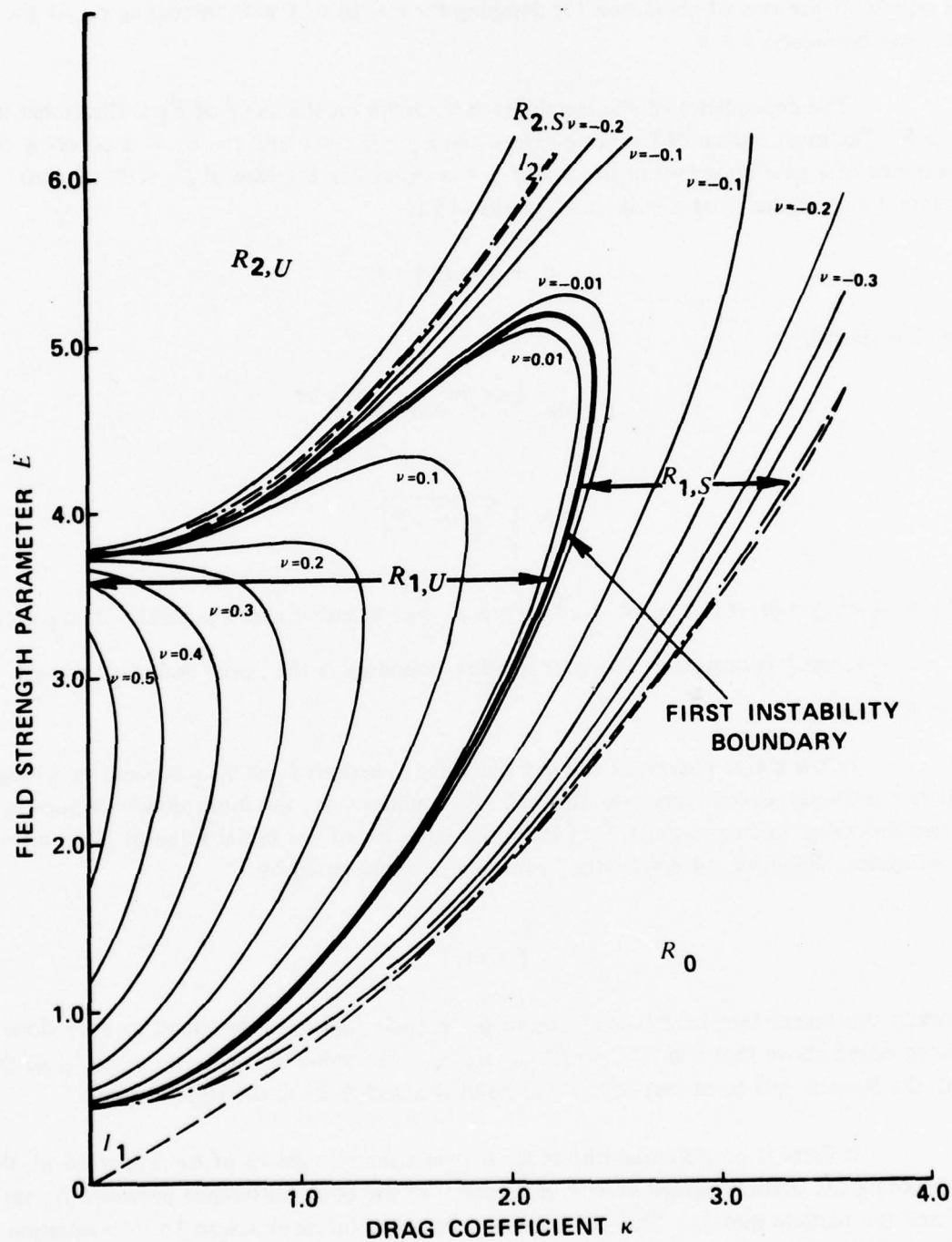


Figure 7. Instability Boundaries

and represents the rate of expansion (or damping for  $\nu < 0$ ) of  $\zeta$  with increasing  $\tau$ . At the instability boundary,  $\nu = 0$ .

The dependence of the instability boundaries on the value of  $E_1$  is illustrated in figure 8. The most radical difference between the  $E_1 = 0$  curve and the  $E_1 \neq 0$  curves is the appearance of a new boundary in the lowest  $\gamma = \alpha$  region for the case of  $E_1 < 0$ . On the horizontal axis of the chart  $E = 0$ , and equation 15 is

$$\zeta'' + \zeta' + E_1 \zeta = 0$$

Then  $\zeta$  is given by

$$\zeta = A e^{-\frac{1}{2}\kappa\tau} e^{\gamma\tau} + B e^{-\frac{1}{2}\kappa\tau} e^{-\gamma\tau}$$

where

$$\gamma = \sqrt{\frac{1}{4}\kappa^2 - E_1}$$

If  $E_1 > \frac{1}{4}\kappa^2$ ,  $\gamma = \beta i$ ; if  $0 < E_1 < \frac{1}{4}\kappa^2$ ,  $\gamma = \alpha < \frac{1}{2}\kappa$ ; in either case  $\zeta$  is stable. If  $E_1 < 0$ ,  $\gamma = \alpha > \frac{1}{2}\kappa$ , and  $\zeta$  is unstable. The new stability boundary is the upper boundary of this unstable region.

In the stable regions of the  $\kappa$ - $E$  chart the functions  $\zeta_1$  and  $\zeta_2$  become vanishingly small as  $\tau$  increases; except very near the stability boundary,  $\zeta_1$ , the more slowly decreasing of the two functions, decreases to  $10^{-6}$  of its initial value (or of the initial value of  $\zeta'$ ) in a few tens of cycles. Equation 14 describing  $\zeta$  can then be represented by

$$\zeta = p(\tau) \tag{20}$$

Physically this means that in the stable region the particle motion is described by  $p(\tau)$  alone. It has been noted above that if  $h = 0$ ,  $p(\tau) = 0$ . Hence if the value of  $E_{dc}$  is set at  $mg/q$ , so that  $h = 0$ , the particle will be at rest at the null point if  $\kappa$  and  $E$  lie in the stable region.

If there is no potential difference between the two sheets of the hyperboloid, the force holding the particle against gravity is supplied by the phase difference between the applied field and the particle motion. This can be shown by substituting equation 16 into equation 13 and integrating with respect to  $\tau$  over one cycle of  $\cos \tau$ . The result is

$$2\pi a_0 E_1 + \pi(a_1 + a_{-1})E + 2\pi h = 0 \tag{21}$$



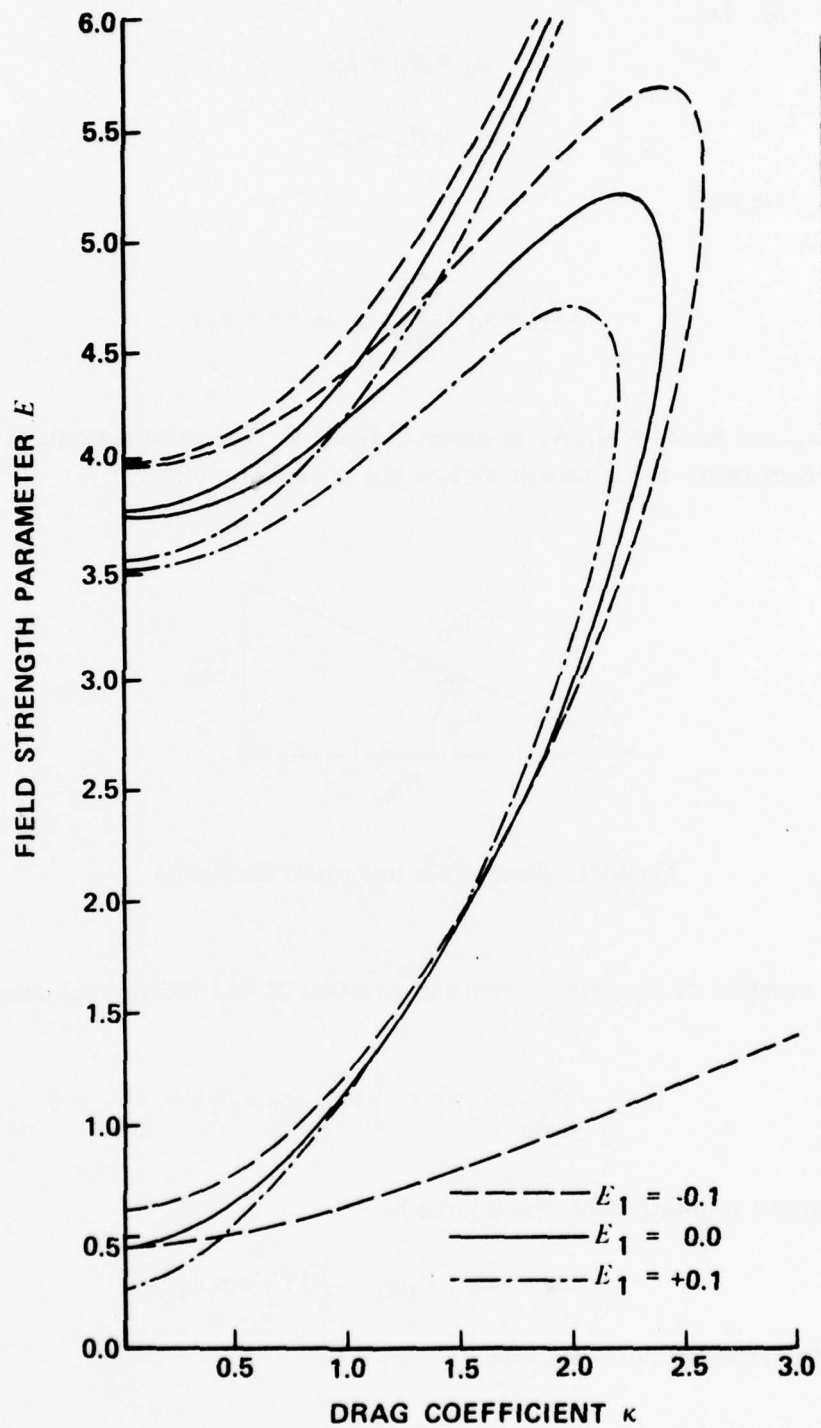


Figure 8.  $E_1$ -Dependence of Instability Boundaries

Note that  $a_n = a_{-n}^*$ . Let

$$a_n = R_n + I_n i$$

$$a_{-n} = R_n - I_n i$$

when  $R_n$  and  $I_n$  are real.

Then

$$p(\tau) = a_0 + \sum_{n=1}^{\infty} C_n \cos(n\tau - \phi_n) \quad (22)$$

where  $C_n = 2|a_n|$  and  $\tan \phi_n = -I_n/R_n$  as shown in figure 9. The phase angle  $\phi_n$  is the angle by which the  $n$ th component of the particle motion lags the driving voltage.

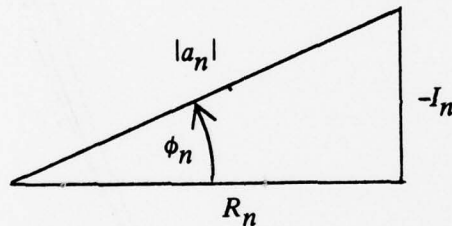


Figure 9. Phase Angle in Particle Oscillation

If equation 21 is written in terms of equation 22 and the physical quantities, it becomes

$$\frac{Cq}{\omega^2 m} \left( a_0 V_1 + \frac{1}{2} V C_1 \cos \phi_1 \right) d + \frac{g}{\omega^2 d} = 0$$

whence the required restoring force,  $mg$ , is given by

$$mg = -Cq \left( V_1 a_0 + \frac{1}{2} V C_1 \cos \phi_1 \right) d$$

We shall consider henceforth only the case  $E_1 = V_1 = 0$ .

Then

$$mg = -\frac{1}{2} Cq (V C_1 \cos \phi_1) d \quad (23)$$

In the case now under consideration, where the constant term in equation 11 is due to gravity alone,  $a_0 < 0$ , and the particle path lies entirely below the null point. The particle position is approximately

$$z = p(\tau)d = [a_0 + C_1 \cos(\omega t - \phi_1)]d \quad (24)$$

and the field strength is approximately

$$E \cong (C|a_0|V \cos \tau)\hat{k} \quad (25)$$

Equation 25 reflects only the oscillation of direction of the field  $E$ . In fact, because the field becomes weaker in the direction of the null point (upward), the particle is in a stronger field when it is below the null point a distance  $|a_0d|$  than when it is above. Equation 23 shows that  $\cos \phi_1$  must be negative. If  $\cos \phi_1 = -1$ , so that  $\phi_1 = \pi$ , equations 24 and 25 show that below the null point the particle is in the stronger part of the field when the field is directed upward, and in the weaker part of the field when the field is directed downward; the net electric force is upward, opposite the force of gravity.

Figure 10 shows the particle depression (the mean distance below the null point of the vibrating particle) when it is being held up only by the null-point ac field. The constant  $c$  is defined by the equation

$$|a_0d| = \frac{Cg}{\omega^2}$$

The quantity  $|a_0d|$  is the particle depression; for a frequency of 60 hertz it is given by the following expression in millimeters:

$$|a_0d| = 0.06895c$$

The dotted lines in figure 10 are the instability boundaries. When  $\kappa$  and  $E$  are such that the general solution described by equation 18 is stable and  $V_{dc} = 0$ , maximum stability corresponds to the minimum particle depression. The electrodynamic quantities that may be varied are the peak voltage  $V$  and the angular frequency  $\omega$ . The curve labeled " $E$  minimum" in figure 10 is the set of  $(\kappa, E)$  pairs for which the particle depression is minimal when  $\kappa$  is constant and  $E$  is varied, i.e., when the frequency is constant and the voltage is varied. If only the frequency is varied, the values of  $\kappa$  and  $E$  for which the particle depression is minimal fall on the curve marked "frequency minimum". These curves are of significance when the particle is first being captured in the chamber before gravity can be overcome by applying the proper voltage  $V_{dc}$  between the two hyperboloidal sheets; when the proper voltage  $V_{dc}$  has been applied, the part of the oscillation described by  $p(\tau)$  vanishes altogether. The particle depression minimum curves can be used to establish chamber design requirements for containment of particles in various size ranges.



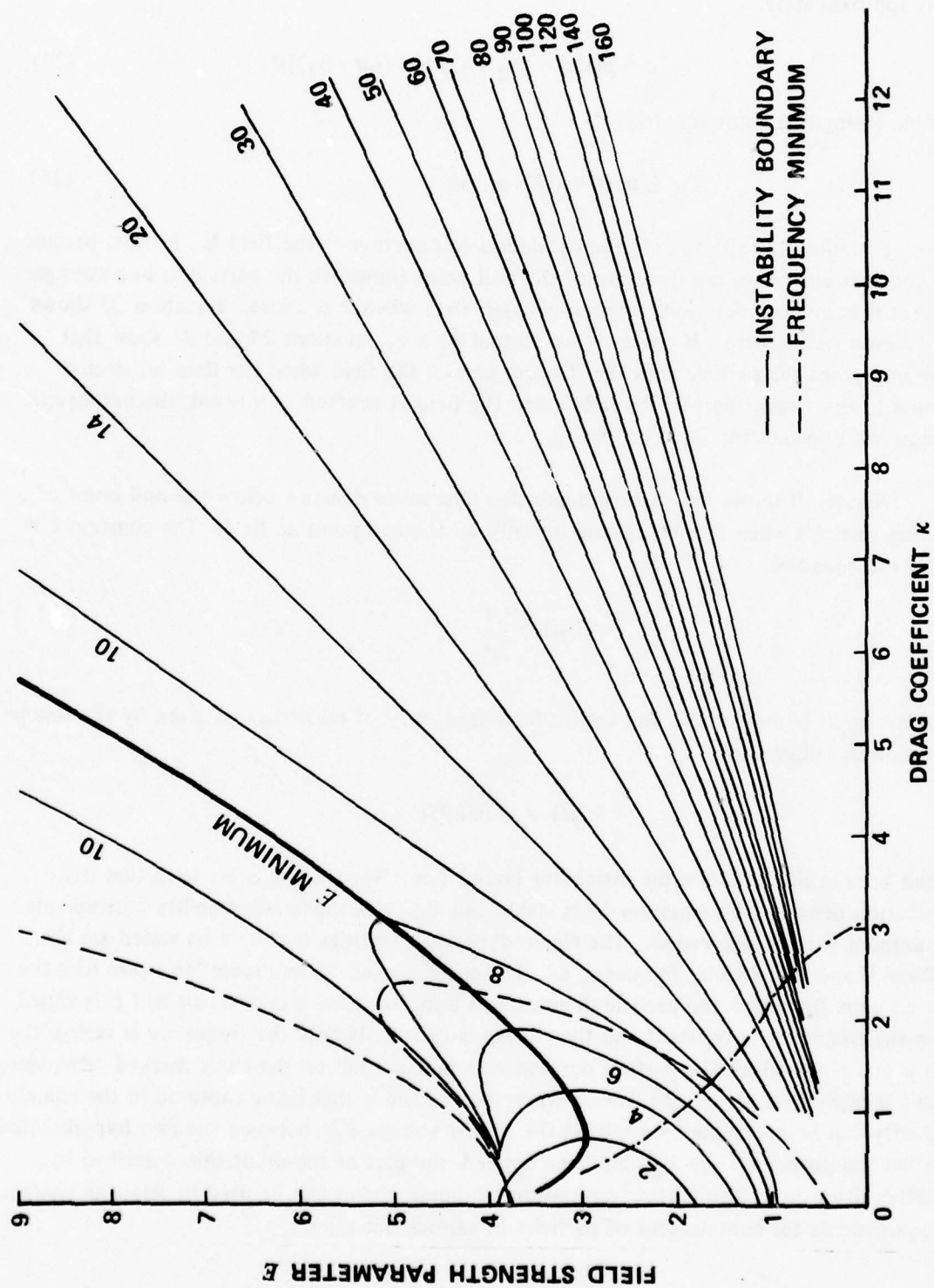


Figure 10. Particle Distance Below Null Point,  $V_{dc} = 0$

We have seen that when  $V_{dc} = 0$  the net electrodynamic force is proportional to the cosine of  $\phi_1$ , the angle by which the fundamental term of the Fourier series  $p(\tau)$  describing the motion of the particle after  $\xi_1$  and  $\xi_2$  are damped out lags the driving voltage  $-V \cos \tau$ . For small values of  $E$

$$\tan \phi \cong -\kappa \quad (26)$$

A quantity related to the lag angle  $\phi_1$  is the value for which

$$p(\tau_0) = p(\tau_0 + \pi) \quad (27)$$

Experimentally this quantity is determined by observing the vibrating particle in the light of a stroboscope flashed twice per cycle of the driving voltage. Two separate images of the particle are observed except when the strobe flash occurs at a point in the cycle for which equation 27 is true, when the two images coincide. From equations 22 and 27

$$a_0 + \sum_{n=1}^{\infty} C_n \cos (n\tau - \phi_n) \approx a_0 + \sum_{n=1}^{\infty} C_n \cos (n\tau + n\pi - \phi_n)$$

whence

$$\sum_{n=0}^{\infty} C_{2n+1} \cos [(2n+1)\tau - \phi_{2n+1}] = 0 \quad (28)$$

If  $E$  is small enough the particle motion is simple harmonic and  $p(\tau)$  can be represented by

$$p(\tau) = a_0 + C_1 \cos (\tau - \phi_1)$$

In this case equation 28 becomes

$$C_1 \cos (\tau - \phi_1) = 0$$

and because if  $C_1$  vanished there would be no electrodynamic force to hold up the particle,

$$\tau_0 \cong \phi_1 \mp \frac{\pi}{2}$$

Then from equation 26,

$$\cot \tau_0 \cong -\tan \phi_1 \cong \kappa$$

For larger values of  $E$ ,

$$\tau_0 = \frac{\pi}{2} + \phi_1 + \frac{C_3}{C_1} \sin \psi_3 + 3 \frac{C_3^2}{C_1^2} \cos \psi_3 \sin \psi_3 - \frac{C_5}{C_1} \sin \psi_5 + \dots$$

where

$$\psi_3 = 3\phi_1 - \phi_3$$

and

$$\psi_5 = 5\phi_1 - \phi_5$$

Figure 11 shows  $\phi_1$  and  $\cot \tau_0$  as functions of  $\kappa$  for several values of  $E$ . Experimental values of  $\cot \tau_0$ , taken from observations on an evaporating particle, are also shown. The value of  $E$  was about 0.26 at the beginning of the observation period when  $\kappa$  was small, but increased markedly toward the end, accounting for the large difference between  $\kappa$  and  $\cot \tau_0$  when  $\kappa$  was large.

When Oseen's Law is used to describe the aerodynamic drag, equation 11 is no longer linear, and the method of continued fractions described in the appendix A is no longer applicable. For this case equation 11 is integrated numerically using Taylor expansions for  $\xi$  and  $\xi'$  and a computer. The principal effect of the velocity squared term is that, in the unstable regions  $R_{1,U}$  and  $R_{2,U}$  of figure 7, the amplitude of the particle vibration does not expand indefinitely as required by the solutions to the linear equation but approaches a constant amplitude. Except near the stability boundary this constant amplitude is reached in a few tens of cycles.

Figure 12 shows the amplitude of vibration (the total length of the path of the particle) as a function of  $E$  for various values of  $\kappa$ , for the case  $h = 0$ . The curves are labelled according to the value of  $\kappa$  to which they correspond. The marks labeled  $LO_x$  and  $UO_x$  represent the intersections of the  $\kappa = x$  line on figure 7 with the lower and upper boundaries of the (odd) instability region  $R_{1,U}$ ;  $LE_x$  and  $UE_x$  designate similar boundaries for  $R_{2,U}$ . The curve labelled  $\kappa = 0.1$  represents a 92- $\mu$ m particle at 60 hertz in air. The amplitude increases from zero starting at  $E = 0.46$ , which is seen from figure 7 to represent the lowest stability boundary. The vibration has a period of  $4\pi$  (twice the period of the driving voltage) as required by the linear solution. The curve rises sharply from the point  $E = 0.46$  and continues past the second stable region ( $E = 3.76$ ) and into the region  $R_{2,U}$ , increasing monotonically. The periodicity in  $R_{2,U}$  is  $4\pi$ , in contrast to the periodicity of  $2\pi$  required by the linear solution in this region. Since the height of the bihyperboloidal chamber for this case is only 190 particle diameters, observation of this mode of vibration for this particle size is extremely difficult.

The curves labeled  $\kappa = 1.0$  represent a 29- $\mu$ m particle in air at 60 hertz. The larger of these curves increases from zero at  $E \cong 1.18$  as required by the linear solution, and the period of vibration is  $4\pi$ . Notice that this curve extends past  $E = 4.2$ , the upper boundary of  $R_{1,U}$ , and

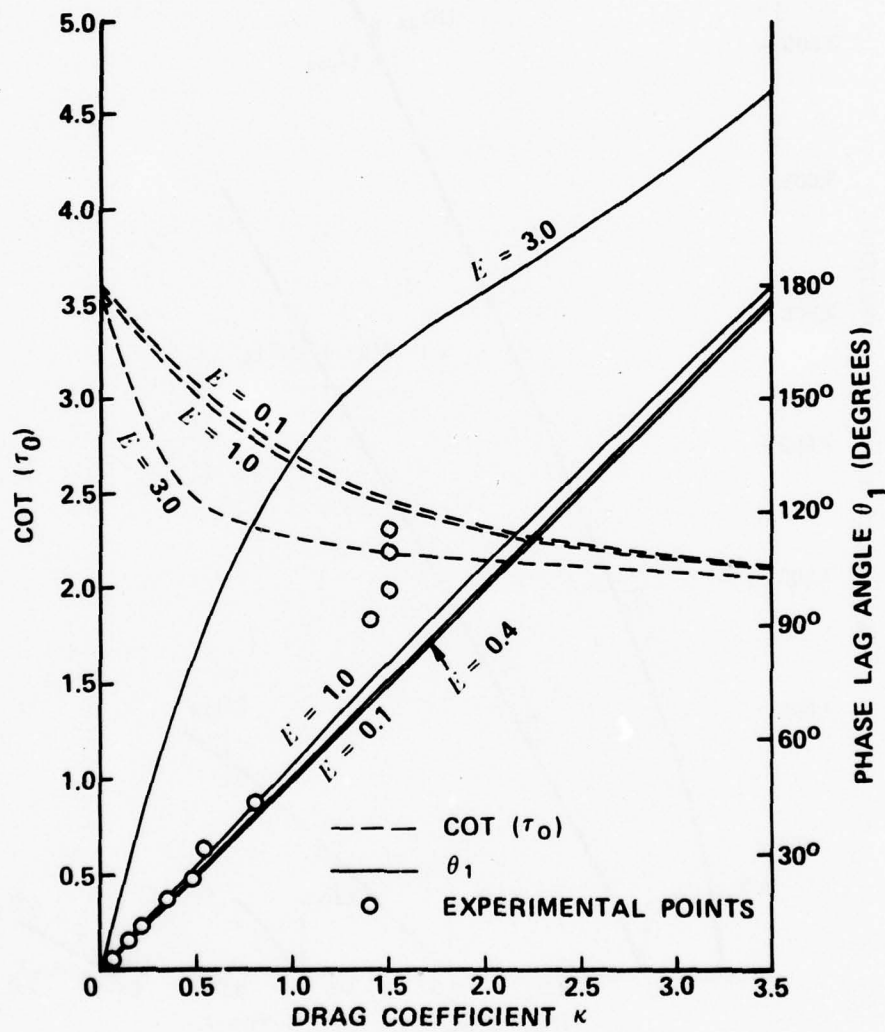


Figure 11. Lag Angle and Coincidence Point

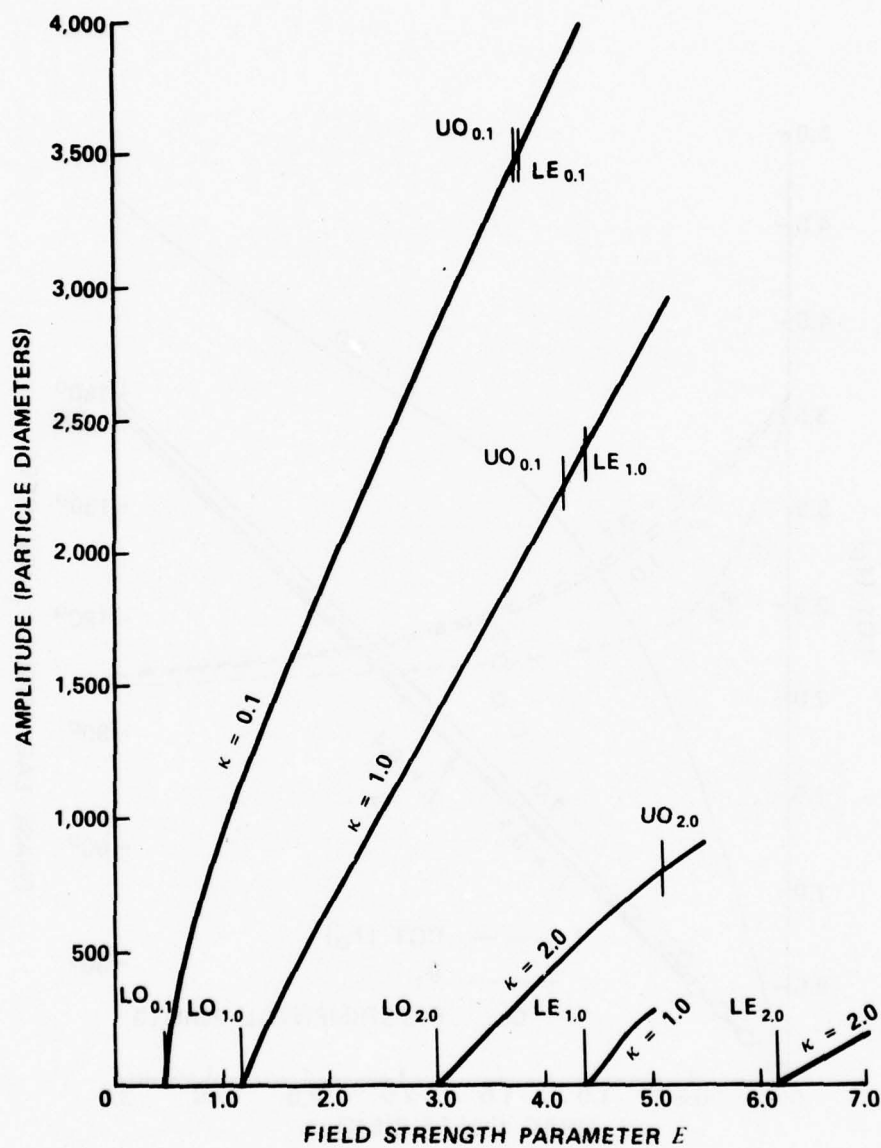


Figure 12. Amplitude of Vibration in Unstable Region



and  $E = 4.4$ , the beginning of  $R_{2,U}$ . Some of the calculated points fell on this extended portion of this curve. Other calculations gave zero amplitude for values of  $E$  lying above the upper boundary of  $R_{1,U}$  or lay on the smaller  $\kappa = 1.0$  curve rising from zero at  $E = 4.4$ , the beginning of  $R_{2,U}$ . The periodicity of points lying on the lower curve is  $2\pi$ , as required by the linear solution. Whether the amplitude calculated for a given value of  $E > 4.2$  lies on the larger or the smaller  $\kappa = 1.0$  curve appears to depend at least in part on the initial values of  $\zeta$  and  $\zeta'$ . The chamber height for this size particle is 600 diameters.

The curve for  $\kappa = 2.0$ , representing a  $21\text{-}\mu\text{m}$  particle, rises comparatively slowly from zero, the value predicted by the linear solution at  $E = 3.0$ , and increases monotonically until  $E = 5.50$ , a value somewhat greater than the value  $E = 5.10$  representing the upper boundary of  $R_{1,U}$ , as determined from the linear equation. The amplitude for  $E = 5.55$ , the next higher value for which a calculation was made, is zero. At  $E = 6.2$ , the lower boundary of  $R_{2,U}$ , the amplitude begins to increase slowly with increasing  $E$ ; the period of vibration is  $2\pi$  on this part of the curve, as required by the linear solutions. Particles of this size ( $20\text{-}\mu\text{m}$ ) and smaller can readily be experimentally observed vibrating in the  $4\pi$ -period mode described here.

The instability curves for horizontal vibration can be seen from equation 12 to be the same as for the vertical vibrations discussed hitherto, with the following exceptions:

(1) For a given value of  $V$ , the signs before  $E$  and  $E_1$  are different from the signs for the vertical case. The sign of  $E$  is immaterial physically, since the phase of  $\tau$  is arbitrary. The difference in the sign before  $E_1$  means that the new instability region that appears for vertical motion when  $E_1$  is negative appears for horizontal motion when  $E_1$  is positive. Therefore, for any given nonzero value of  $E_1$ , there is an unstable region at the bottom of the  $\kappa$ - $E$  chart either for vertical motion or for horizontal motion.

(2) The coefficients  $E$  and  $E_1$  are multiplied by one-half. This means that corresponding points on the chart require twice as much alternating voltage for the horizontal component of motion as for the vertical component. Hence for values of  $\kappa$  less than about 1.8, the horizontal and the vertical instability regions overlap; while for values of  $\kappa$  greater than 1.8, there is a region of horizontal double-period oscillation lying somewhat above the first vertical instability region and overlapping the second (single-period oscillation) vertical instability region.

(3) With the axis of the chamber vertical, there is no term corresponding to  $h$ . Hence there is no horizontal equivalent to the part of the motion described by  $p(\tau)$ .

A number of phenomena that can be correlated with the theoretical discussion have been observed experimentally. Generally, when  $\kappa$  and  $E$  lie outside the unstable regions, and  $V_{dc} = 0$ , the particle is observed to oscillate below the null point with the frequency of the driving voltage (60 hertz in this case), as described by equation 20. When the weight of the

particle is balanced electrostatically by setting  $V_{dc}$  at the proper value, the particle is observed to come to rest at the null point; this corresponds to the fact that  $h$  vanishes in this case, and because all coefficients of  $p(\tau)$  are proportional to  $h$ ,  $p(\tau)$  also vanishes.

The charge-to-mass ratio of the particle is found by electrostatically balancing the particle at the null point; it is given by

$$\frac{q}{m} = \frac{g}{C_{dc}V_{dc}}$$

where  $V_{dc}$  is the voltage necessary to balance the particle. The value of  $E$  for any particular setting of the alternating voltage  $V$  is then

$$E = \frac{C_g}{C_{dc}\omega^2} \frac{V}{V_{dc}}$$

The value of  $C_{dc}$  has not been calculated geometrically for the hyperboloidal chamber; it was found experimentally to be  $17.7 \pm 0.1 \text{ meter}^{-1}$ , as described later in this report. Then for any particle for which  $V_{dc}$  has been measured,  $E$  corresponding to the alternating voltage is

$$E = 0.0210 \frac{V}{V_{dc}}$$

When particles of any diameter over  $19 \mu\text{m}$  were balanced at the null point and made to oscillate by increasing the alternating voltage  $V$ , the oscillation was invariably in the double-period mode required by the theory, and the values of experimental quantities were consistent with the values of  $E$  and  $\kappa$  in the calculated stability boundaries.

The increase in amplitude of oscillation with increasing alternating voltage was large for large particles — so large that it was virtually impossible to maintain large particles ( $>75 \mu\text{m}$ ) in this mode. For smaller particles the increase in amplitude was less marked; particles of  $20\text{-}\mu\text{m}$  diameter or less could be held stably at any point in the instability region. These observations are consistent with the calculations summarized in figure 10.

Particles of  $18.5\text{-}\mu\text{m}$  diameter or less could not be made to oscillate horizontally in the double-period mode. For these particles,  $\kappa > 2.5$ ; figure 7 shows that the first unstable region does not extend this far to the right, so double-period vibration is not to be expected.

When the alternating voltage was just below that required to produce constant-amplitude, double-period oscillations, and the laboratory table was jarred, a double-period oscillation that disappeared in a few seconds was observed; the jarring of the table introduced a new set of initial conditions and new values of  $A$  and  $B$  in equation 14, so that the amplitude of the  $\xi_1$  and  $\xi_2$  functions became appreciable. The function  $\xi_2$  described in equation 18 no doubt damped out almost instantaneously, but because near the boundary  $|\nu| = |\gamma - \kappa/2|$  is very small, the time required for  $\xi_1$  to damp out and become negligible was long enough for the oscillation to be observed.

One calculated result not observed experimentally is shown in figure 12. Calculation based on Oseen's Law indicated that for a  $21\text{-}\mu\text{m}$  particle ( $\kappa = 2.0$  in air at 60 hertz), as the alternating voltage is raised above the value required to produce double-period oscillation, the amplitude should rise monotonically until  $E$  is somewhat above the upper boundary of  $R_{1,U}$ , and then drop suddenly. Qualitative observations of  $20\text{-}\mu\text{m}$  particles seemed to show that the amplitude reaches a peak somewhere in the  $R_{1,U}$  region and then decreases gradually with increasing voltage. That Oseen's modification of Stokes' Law is itself an approximation may account for this discrepancy.

## B. Experimental Verifications.

### 1. Verification of the Instability Boundary Curve.

A 50% solution of glycerine and water was placed in the capillary described in section II. A single particle was selected and inserted into the chamber. Figure 13 is a photograph of a suspended glycerine particle.

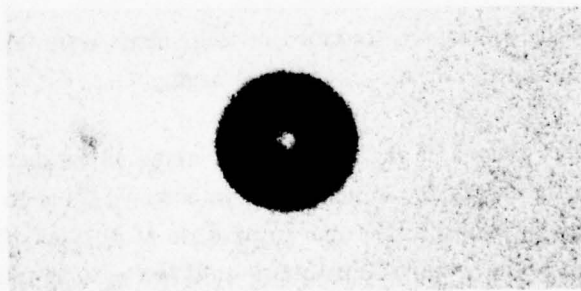


Figure 13. A Suspended Glycerine Particle  $80\text{ }\mu\text{m}$  in Diameter  
Focusing of the backlight by the particle itself causes the central white spot.



The water solution was used because it accepted more charge than pure glycerine. The water quickly evaporated leaving an almost pure glycerine particle that was highly charged.

Glycerine was chosen as the calibrating material for several reasons. First, it is liquid at operating temperature. As a result, the particle is spherical due to surface tension. Therefore, the diameter  $d$  is an actual value rather than an average value, making the calculation of  $\kappa$  more accurate. Second, glycerine is soluble in water, yet not highly hygroscopic. Hence water, used to obtain a more highly charged particle, could be more easily removed by placing the particle in a low-humidity chamber. Finally, the vapor pressure of glycerine is appropriate for the time frame required to make these measurements.

The ideal situation for calibration was to maintain a decreasing evaporation rate so that the rate of change of the particle diameter remained approximately  $10\text{ }\mu\text{m/hr}$ . Glycerine particles  $100\text{ }\mu\text{m}$  in diameter would evaporate far too slowly at room temperature. Therefore, the chamber was heated at the beginning of the run and then slowly cooled during the time the measurements were made. Because of this procedure the evaporation rate decreased as the temperature decreased, and thereby a fairly constant rate of change of the particle diameter was maintained. In addition, this procedure eliminated thermally induced convection currents.

Typical runs started with a  $100\text{-}\mu\text{m}$ -diameter particle at  $55^\circ\text{C}$  and ended with a  $10\text{-}\mu\text{m}$ -diameter particle at  $30^\circ\text{C}$ . Measurements were taken at various time intervals during the run. The procedure consisted of several steps. First, the flow of dry air was shut off. Next, the diameter of the particle was determined using the calibrated image-splitting eyepiece. The particle was then balanced by varying the dc voltage until the two images of the particle, formed by operating the stroboscope at 120 flashes per second, coincided. The dc voltage was then recorded on the visicorder and oscilloscope. Next, the ac splitting voltage was determined and recorded on both the visicorder and the oscilloscope. Finally, the temperature was recorded on the visicorder.

Because all of the previously described measurements were taken within 1 minute, changes in the particle during the measurement were negligible.

From elementary theory, if the ac voltage is increased to, or becomes greater than, the value obtained from the instability boundary curve corresponding to a particular particle diameter and density, the particle should begin to oscillate at one-half the driving frequency  $\omega$ , with increasing amplitude. The amplitude increases until the particle impacts on one of the electrodes. As a result, it appears as if measuring the ac splitting voltage requires losing the particle.

Because of nonlinear effects not described by Stokes' Law, this was not the case. At the instability boundary the particle did begin to oscillate in the  $\omega/2$  mode. However, the amplitude did not increase with time until the ac voltage was increased beyond the stability boundary. As a result the ac splitting voltage could be measured without losing the particle by noting the sharp transition point to the  $\omega/2$  mode.

Figure 14 is a graph of the theoretically calculated instability boundary. This boundary, as shown in the theoretical section, is independent of chamber design. The curve is plotted in this figure with  $E$  and  $d$  coordinate axes. Actually the boundary is a function of  $E$  and  $\kappa$  as previously shown. However, the diameter  $d$ , may be related to  $\kappa$  by the equation

$$d = \left( \frac{18\eta}{\kappa\rho\omega} \right)^{\frac{1}{2}}$$

where the variables, previously described, were applied to the case of a suspended glycerine particle.

Superimposed on this graph are experimental data points computed from the formula

$$E_0 = \frac{C_{ac}gV_{ac}}{C_{dc}\omega^2V_{dc}}$$

using the actual diameter  $d$  in micrometers.

In summary, for calculating data points or the theoretical curve,  $g$ ,  $\omega$ ,  $\eta$ , and  $\rho$  were known constant values.<sup>9</sup> For the data points,  $V_{ac}$ ,  $V_{dc}$ , and  $d$  were experimentally determined, whereas for the theoretical curve these variables were allowed to assume a continuous range of values.

The effect of chamber design was included by means of the parameters by  $C_{ac}$  and  $C_{dc}$ , the electric field linearity constants. Ideally, both parameters could be calculated theoretically from the shape of the electrodes. In fact,  $C_{ac}$  was easily calculated (as shown in section III. A), but the calculation of  $C_{dc}$  failed in spite of many approaches attempted, and hence,  $C_{dc}$  was experimentally determined. Section III. A shows that for large particles,  $E$  limits to a constant value of 0.464. By measuring  $V_{ac}/V_{dc}$  for many glycerine particles with a diameter greater than 110  $\mu\text{m}$  and by knowing  $C_{ac}$ ,  $g$ , and  $\omega$ , the quantity  $C_{dc}$  was determined to be  $17.7 \pm 0.1$  meter<sup>-1</sup>.

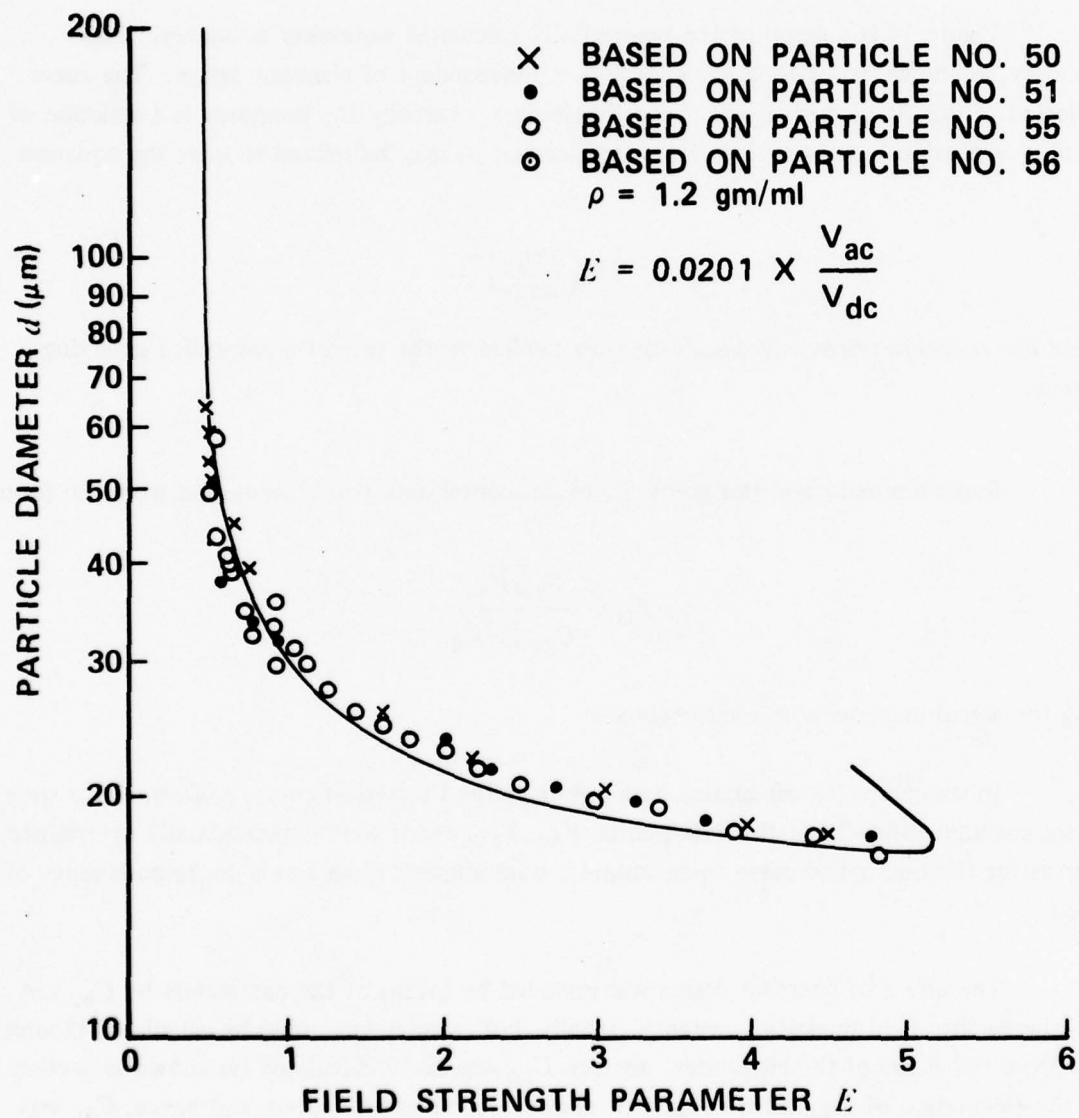


Figure 14. Instability Boundary Curve

## 2. Rate of Instabilization and the $\omega/2$ Boundary.

As already mentioned, because of nonlinear effects not described by Stokes' Law, a particle maintains stable oscillation beyond the instability boundary. After the boundary is crossed, the particle oscillates with increasing amplitude in the  $\omega/2$  mode. If Stokes' Law were obeyed, the amplitude would continue to increase and the boundary would be a true instability boundary. However, as shown in the theoretical section, nonlinear drag effects become important even for small amplitudes and velocities of oscillation. The nonlinear theory predicts that the displacement amplitude increases to some value and then becomes constant. Therefore the boundary is actually a quasi-instability boundary. For a given percent increase in  $E$  beyond the boundary, the theory also predicts that larger particles have larger constant amplitudes than smaller particles in the same state.

Experimentally it was found that for larger particles, ac voltage increases beyond the splitting voltage cause large-amplitude changes. This is not true for smaller particles. Although quantitative measurements were not made, this phenomenon is completely consistent with the theoretical results concerning the rate of instabilization.

In summary, the instability boundary is actually the boundary at which  $\omega/2$  frequency oscillation begins to appear. Because of nonlinear drag effects, oscillation at this frequency stabilizes at an amplitude that is a function of the value of  $E$  above the instability boundary. In this sense the boundary is not a true instability boundary.

Although the  $\omega/2$  frequency oscillation begins to appear at this boundary, the instability boundary is not the point at which the  $\omega/2$  frequency is allowed. As shown in the theoretical section, the  $\omega/2$  boundary is an entirely different curve. However, oscillation in the  $\omega/2$  mode is damped and not visible until the instability boundary is crossed.

Experimentally it was found that after the  $\omega/2$  boundary has been crossed, but before the instability boundary has been crossed, the particle oscillates only in the  $\omega$  mode (if unbalanced). On the other hand, if the particle is balanced and then subjected to a vibration, it then oscillates in the  $\omega/2$  mode until the motion has been eliminated by damping. Experimentally it was also found that the degree of  $\omega/2$  mode damping lessens as one approaches the instability boundary; this is also consistent with theoretical results.

## 3. Passing Through the First Instability Region.

From the theoretical description, it was noted that the first instability region is bounded and separated from a second instability region. When the value of  $E$  increases from zero, a particle starts in a stable state, passes through an unstable region, and finally ends in a stable region of motion.



It appears that the requirement of passing through the primary instability region would prohibit observing the top portion of the first instability boundary. However, because of the quasi-instability character of the boundary as a result of nonlinear drag effects, a particle with a diameter of 20- $\mu\text{m}$  or less passes through this region. In other words, the constant amplitude of motion in the  $\omega/2$  mode did not exceed the distance between the top and bottom sheets of the hyperboloid for this particle diameter.

When smaller particles were used, the top portion of the first boundary was easily observed. Starting in the first stable region, as the ac voltage was increased, the particle began to oscillate in the  $\omega/2$  mode, indicating that the first boundary had been reached. As higher voltages were applied, larger amplitude oscillations were observed. Finally the amplitude decreased to zero indicating that the top portion of the first instability region had been crossed. Further increase of the ac voltage resulted in lower values of the restoring force as the second instability region was approached. At the second boundary there was no restoring force at all. As a result, this boundary was never experimentally observed.

At a particle diameter of 18.5  $\mu\text{m}$  or less there was no first instability boundary. In this case it was observed that the ac voltage could be varied over a large range of values. In this region ( $\kappa > 2.4$ ) as the ac voltage was increased the particle would move toward the null point until a certain voltage was attained. If a further increase of voltage were applied, the particle would then move away from the null point. This indicated that the net restoring force reached a maximum as the ac voltage was increased with this maximum being dependent on the particle size as shown in figure 10.

#### 4. Phase Angle.

As mentioned in the introduction and described in detail in section III.A, the phase angle between the ac voltage oscillation and the particle oscillation was the basic parameter in accounting for the nonzero time-averaged force toward a point in space experienced by the particle. The value of the phase angle varied with different-sized particles and could have been used to measure particle diameter.

Experimental measurement of the phase angle was accomplished by flashing the stroboscope at 120 hertz. The time-delay attachment to the stroboscope was varied until the two images of the particle coincided, at which point the stroboscope was flashing in phase with the particle motion. The phase angle was then determined from the displaying of the ac voltage and the stroboscope flash on a two-channel oscilloscope.

As shown in section III.A (figure 11), actual phase angle measurements made for the bihemispheric system with a 50% solution of water and ethylene glycol were in excellent agreement with the calculated values. However similar phase angle measurements were not made for the bihyperboloidal system described in this report.



## 5. Particle Discharge.

Particle discharge has been investigated and reported by others<sup>6</sup>. In theory particle discharge should occur when the electrostatic force, which increases during evaporation of the droplet as the charge-to-mass ratio increases, equals the surface tension force. This condition is commonly known as the Rayleigh stability limit. The nature of particle discharge has been described as the ejection of several small highly-charged droplets comprising about 30% of the electric charge and 5% of the mass of the original droplet.

In practice particle discharge was noted by the sudden disappearance of the droplet. If the ac voltage was high enough to contain the particle, the particle could be returned to the field of view by increasing the dc voltage. The illumination from the stroboscope was not sufficient to distinguish any small ejected droplets; however, the electrical measurements on the large droplet after discharge indicated a 20% to 40% loss of charge. The 5% decrease in mass could not be measured accurately because of the time required for rebalancing the particle to compensate for the charge loss.

In the chamber at the time of discharge, the forces should be related by

$$\sigma = \frac{3.768\rho^2 d^3}{C_{dc}^2 V_{dc}^2}$$

where  $\sigma$  is the surface tension and the right-hand side is the electrostatic force. Calculations for several droplets were made from the data just prior to discharge of the droplet. These results varied considerably from the measured surface tension of the bulk liquid (63 dynes/cm) and ranged in value from 20 to 50 dynes/cm. No apparent reason for this wide range of values has been determined.

## 6. Charge Decay Due to Cosmic Ray Ionization.

One source of interest and possible error was the rate of loss of charge due to cosmic ray ionization. A polyethylene bead, 66.7  $\mu\text{m}$  in diameter, was placed in the chamber and suspended for 68 hours. Loss of charge was indicated by an increase in the dc balancing voltage. The measured rate of increase was approximately  $1.76 \times 10^{-5}$  volts/second.

With dry air circulating through the chamber, the atmosphere was free of contaminants. A logical explanation of the discharge seemed to be ionization caused by cosmic ray radiation.

The rate of ion-pair production at sea level is 1.5 to 2 ion pairs per sec-cm<sup>3</sup>.<sup>10</sup> These ions are small and have a mobility of about 2 cm<sup>2</sup>/(v-sec). Thus they can only exist within the chamber, impinging on the chamber walls or on the particle, for less than one-half of a cycle of the ac voltage.

Calculations showed that the charge on the polyethylene particle was approximately  $1.8 \times 10^{-12}$  coulombs. It was found that the electric field due to the particle equaled the ac field at a distance of 0.5 cm from the particle. Based on this fact and the design of the chamber, one would expect that, during one-half of a cycle, ions contained in a disk 2.50 cm in diameter and 1 cm in length and ions contained in a cylinder 3.50 cm in length and 1 cm in diameter, both coaxial with the symmetry axis of the chamber, would impinge on the particle. Thus the rate of discharge would be approximately 2.9 to 3.9 electronic charges per second. (Note that one-half of the ion pairs produce a discharge for one-half of a cycle.)

From the relation

$$\frac{dq}{dt} = \frac{mg}{C_{dc}} V_{dc}^2 \frac{dV_{dc}}{dt}$$

where all the quantities have been previously described, the rate of increase of  $V_{dc}$  was found to correspond to a discharge rate of 3.8 electronic charges per second.

## LITERATURE CITED

1. Straubel, H. *Naturwissenschaften* 42, 506 (1955).
2. Straubel, H. Die Dosierung von Substanzmengen unter  $10^{-6}$  g. mittels elektrostatischer Aufladung für Zwecke der Mikroanalyse. *Z. Elektrochem.* 60, (9/10), 1033-1036 (1956).
3. Wuerker, R. F., Shelton, H., and Langmuir, R. V. Electrodynamic Containment of Charged Particles. *J. Appl. Phys.* 30, No. 3, 342-349 (1959).
4. Müller, A. Theoretische Untersuchungen über das Verhalten geladener Teilchen in Sattelpunkten elektrischer Wechselfelder. *Ann. Phys.* 7, (6), 206-220 (1960).
5. Fansler, K. S., Frickel, R. H., Wright, R. J., and Eppes, H. W. Sublimation of Electrically Charged Particles. EATM 141-2. September 1968. UNCLASSIFIED Report.
6. Schweizer, J. W., and Hanson, D. N. Stability Limit of Charged Drops. *J. Colloid and Interface Sci.* 35, (3), 417-423 (1971).
7. Ataman, S., and Hanson, D. N. Measurement of Charged Drops. *Ind. Eng. Chem.* 8, 833-836 (1969).
8. Owe Berg, T. G., and Gaukler, T. A. Apparatus for the Study of Charged Particles and Droplets. *Am. J. Phys.* 37, (10), 1013-1018 (1969).
9. CRC Handbook of Chemistry and Physics. Robert C. Weast (ed.). The Chemical Rubber Co., Cleveland, OH. 1969.
10. American Institute of Physics Handbook. Dwight E. Gray (ed.). McGraw-Hill, New York, NY. 1957.
11. McLachlan, N. W. Theory and Application of Mathieu Functions. Oxford University Press, Oxford. 1951.
12. Morse, P. M., and Feshbach, H. Methods of Theoretical Physics. McGraw-Hill, New York. 1953.

# APPENDIX A DERIVATION OF COEFFICIENTS

The relation between equation 15

$$\zeta''(\tau) + \kappa \zeta' + (E_1 + E \cos \tau) \zeta(\tau) = 0 \quad (15)$$

and the Mathieu equation

$$\bar{\zeta}''(\bar{\tau}) + (\bar{a} - 2\bar{q} \cos 2\bar{\tau}) \bar{\zeta}(\bar{\tau}) = 0 \quad (A-1)$$

is described, for instance, in reference 11.

Let

$$\tau = 2\bar{\tau}$$

$$\zeta = e^{-\kappa\bar{\tau}} \bar{\zeta}$$

Then

$$\zeta'(\tau) = \frac{1}{2} e^{-\kappa\bar{\tau}} (\bar{\zeta}' - \kappa\bar{\zeta}) \quad (A-2)$$

$$\zeta''(\tau) = \frac{1}{4} e^{-\kappa\bar{\tau}} [\bar{\zeta}'' - 2\kappa\bar{\tau}' + \kappa^2\bar{\zeta}]$$

Substituting equation A-2 into equation 15 yields

$$\bar{\zeta}''(\bar{\tau}) + (4E_1 - \kappa^2 + 4E \cos 2\bar{\tau}) \bar{\zeta}(\bar{\tau}) = 0$$

This is equation A-1 where

$$\bar{a} = 4E_1 - \kappa^2 \quad (A-3)$$

$$\bar{q} = -2E$$

as described in reference 11.

The solutions to equation A-1 are of the form

$$\bar{\xi}_1 = e^{\bar{\gamma}\bar{\tau}} \sum_{n=-\infty}^{\infty} \bar{b}_n e^{2in\bar{\tau}} \quad (\text{A-4})$$

$$\bar{\xi}_2 = e^{-\bar{\gamma}\bar{\tau}} \sum_{n=-\infty}^{\infty} \bar{b}_n e^{-2in\bar{\tau}}$$

where  $\bar{\gamma}$  takes one of the forms

$$\bar{\gamma} = \bar{\alpha}$$

$$\bar{\gamma} = \bar{\alpha} + i \quad (\text{A-5})$$

$$\bar{\gamma} = \bar{\beta}i$$

where  $\bar{\alpha}$  and  $\bar{\beta}$  are real and  $\alpha$  is nonnegative.

From equations 17, A-4, and A-5 it is evident that the solutions of equation 15 are

$$\xi_1 = e^{-\frac{1}{2}\kappa\tau} e^{\gamma\tau} \sum_{n=-\infty}^{\infty} b_n e^{in\tau}$$

$$\xi_2 = e^{-\frac{1}{2}\kappa\tau} e^{-\gamma\tau} \sum_{n=-\infty}^{\infty} b_n e^{-in\tau}$$

where  $\gamma$  may be of the form  $\gamma = \alpha$ ,  $\gamma = \alpha + \frac{1}{2}i$ , or  $\gamma = \beta i$  for real  $\alpha$  and  $\beta$ .

The values of  $\bar{\alpha}$  and  $\bar{\beta}$  as functions of  $a$  and  $q$  have been calculated and are displayed, e.g., in reference 11, as Ince's chart. It is possible to take values from Ince's chart and use them for the chart shown in figure 7 via equations 17 and A-3. In this investigation, however, calculations were made directly from equations 15 and 18 by the method of continued fractions described in references 11 and 12.

The solution to the inhomogeneous form of equation 15 given by equation 13

$$\xi'' + \kappa\xi' + (E_1 + E \cos \tau)\xi + h = 0 \quad (13)$$



contains a third term having the same periodicity as  $\cos \tau$ ; the entire solution is thus given by equation 14, using equation 16, i.e.,

$$\zeta(\tau) = A\zeta_1(\tau) + B\zeta_2(\tau) + p(\tau) \quad (14)$$

where

$$p(\tau) = \sum_{n=-\infty}^{\infty} a_n e^{in\tau} \quad (16)$$

The function  $p(\tau)$  was also calculated by the method of continued fractions.

To solve for the coefficients in equation 16 let

$$\zeta = p(\tau) = \sum_{n=-\infty}^{\infty} a_n e^{in\tau}$$

then

$$\zeta' = \sum_{n=-\infty}^{\infty} i n a_n e^{in\tau}$$

$$\zeta'' = \sum_{n=-\infty}^{\infty} -n^2 a_n e^{in\tau}$$

and, because  $\cos \tau = \frac{1}{2}(e^{i\tau} + e^{-i\tau} + e^{-i\tau})$  equation 13 becomes

$$h + \sum_{n=-\infty}^{\infty} [a_n(-n^2 + in\kappa + E_1)e^{in\tau} + \frac{E}{2}a_n(e^{i(n+1)\tau} + e^{i(n-1)\tau})] = 0 \quad (A-6)$$

The coefficient of  $e^{in\tau}$  in the left side of equation A-6 must vanish for each value of  $n$ , whence

$$a_n(E_1 - n^2 + in\kappa) + \frac{E}{2}a_{n-1} + \frac{E}{2}a_{n+1} = 0 \quad (\text{if } n \neq 0) \quad (A-7)$$

and

$$E_1 a_0 + \frac{E}{2}a_{-1} + \frac{E}{2}a_1 + h = 0 \quad (A-8)$$

Let  $r_n$  be defined by

$$r_n = \frac{a_n}{a_{n-1}} \quad (A-9)$$

Then equation A-7 can be written as

$$(E_1 - n^2 + in\kappa) + \frac{E}{2} \frac{1}{r_n} + \frac{E}{2} r_{n+1} = 0 \quad (\text{A-10})$$

whence

$$r_n = \frac{1}{\frac{2}{E} (n^2 - E_1 - in\kappa) - r_{n+1}} \quad (\text{A-11})$$

If  $\bar{r}_n$  is

$$\bar{r}_n = \frac{a_{-n}}{a_{-(n-1)}} \quad (\text{A-12})$$

equation A-10 yields

$$\bar{r}_n = \frac{1}{\frac{2}{E} (n^2 - E_1 + in\kappa) - \bar{r}_{n+1}} \quad (\text{A-13})$$

It is evident that for any value of  $n_0$ ,  $r_{n_0}$  can be expressed as a continued fraction in terms of  $r_n$  where  $n > n_0$ .

To assume that the series representing  $p(\tau)$  converges, we require that for some value of  $n_0$ ,  $|r_n|$  and  $|\bar{r}_n|$  be less than some upper bound if  $n > n_0$ . Then for large enough  $n_1$

$$|r_{n_1} + 1| \ll \frac{2}{E} |n_1^2 - E_1 - in\kappa|$$

and

$$|\bar{r}_{n_1} + 1| \ll \frac{2}{E} |n_1^2 - E_1 + in\kappa| \quad (\text{A-14})$$

For  $n = n_1$ , equation A-11 may be written

$$r_{n_1} = \frac{1}{\frac{2}{E} (n_1^2 - E_1 - in_1\kappa)}$$

$$\bar{r}_{n_1} = \frac{1}{\frac{2}{E} (n_1^2 - E_1 + in_1\kappa)} \quad (\text{A-15})$$

Using these values of  $r_{n_1}$  and  $\bar{r}_{n_1}$ ,  $r_{n_1-1}$  and  $\bar{r}_{n_1-1}$  may be calculated from equation A-11. In the same way values of  $r_n$  and  $\bar{r}_n$  may be calculated for successively lower values of  $n$ , until  $r_1$  and  $\bar{r}_1$  have been found. Equations A-15 show that, since  $E$ ,  $n$ ,  $E_1$ , and  $\gamma$  are real,  $\bar{r}_{n_1} = r_{n_1}^*$ ; equations A-11 and A-13 show that if  $r_{n+1} = \bar{r}_n^* + 1$ , then  $r_n = \bar{r}_n^*$ . Hence

$$\bar{r}_n = r_n^* \quad (\text{A-16})$$

for all  $n$ , and only the  $r_n$  need be calculated.

From equations A-9, A-12, and A-16

$$a_1 = r_1 a_0$$

and

$$a_{-1} = r_1^* a_0$$

whence equation A-8 can be written

$$a_0[E_1 + ER(r_1)] + h = 0 \quad (\text{A-17})$$

or

$$a_0 = - \frac{h}{E_1 + ER(r_1)}$$

where  $R(r_1)$  is the real part of  $r_1$ . The value of  $a_0$ , the mean position of the particle with respect to the null point, is real, as it must be, being a physical quantity. Then  $R(a_1) = a_0 R(r_1)$  and equation A-17 can be written

$$ER(a_1) + h + a_0 E_1 = 0$$

This equation is essentially equation 21 reached in a different way.

Starting from equation A-18, successive coefficients of  $p(\tau)$  may be calculated as

$$a_{n+1} = r_{n+1} a_n$$

$$\bar{a}_{n+1} = a_{n+1}^*$$

In actual calculation, the starting value of  $n$  need not be so high that equation A-14 applies; the error in  $r_n$  decreases very rapidly as  $n$  decreases. For  $E < 10$ , the value of  $n_1$  need exceed by no more than 10 the highest value of  $n$  for which an accurate value of  $a_n$  is required.

In order to determine the value of  $\gamma$  in equation 18, the expression for  $\xi_1$  is substituted into equation 15 yielding

$$\sum_{n=-\infty}^{\infty} e^{in\tau} e^{(\gamma - \frac{1}{2}\kappa)\tau} [(\gamma^2 - \frac{1}{4}\kappa^2 - n^2 + E_1 + 2in\gamma)b_n + \frac{E}{2}(b_{n+1} + b_{n-1})] = 0$$

whence

$$(b_{n+1} + b_{n-1}) - \frac{2}{E} (n^2 + \frac{1}{4}\kappa^2 - \gamma^2 - E_1 - 2in\gamma)b_n = 0 \quad (\text{A-19})$$

Let  $r_n$  and  $\bar{r}_n$  be

$$r_n = \frac{b_n}{b_{n-1}}$$

and

$$\bar{r}_n = \frac{b_{-n}}{b_{-(n-1)}}$$

respectively.

Then equation A-19 is

$$\frac{1}{r_n} + r_{n+1} = \frac{2}{E} (n^2 + \frac{1}{4}\kappa^2 - \gamma^2 - E_1 - 2in\gamma)$$

$$r_n = \frac{1}{\frac{2}{E} (n^2 + \frac{1}{4}\kappa^2 - \gamma^2 - E_1 - 2in\gamma) - r_{n+1}} \quad (\text{A-20})$$

$$\bar{r}_n = \frac{1}{\frac{2}{E} (n^2 + \frac{1}{4}\kappa^2 - \gamma^2 - E_1 + 2in\gamma) - \bar{r}_{n+1}} \quad (\text{A-21})$$

As before,  $r_{n+1}$  is regarded as negligible for some sufficiently large value of  $n$ , and  $r_n$  and  $\bar{r}_n$  are calculated for successively lower  $n$ . For  $n = 0$ , equation A-19 is

$$r_1 + \bar{r}_1 = \frac{2}{E} (\frac{1}{4}\kappa^2 - \gamma^2 - E_1) \quad (\text{A-22})$$

In general, equation A-22 is not true. If any three of the four quantities  $E$ ,  $E_1$ ,  $\kappa$ , and  $\gamma$  are known, a value of the fourth quantity must be sought for which equation A-22 is satisfied. In this investigation the entities to be determined were boundaries between various regions and curves of constant value of  $\nu$ , where

$$\nu = \alpha - \frac{1}{2}\kappa$$

in regions where  $\gamma \neq 0$ .

On these curves

$$\gamma = \nu + \frac{1}{2}\kappa$$

or

$$\gamma = \nu + \frac{1}{2}\kappa + \frac{1}{2}i$$

On periodicity boundaries between regions where  $\gamma = \alpha$  and  $\gamma = \beta i$ , it is evident that unless  $\gamma$  is a discontinuous function of  $\kappa$  and  $E$ ,

$$\gamma = 0$$

On periodicity boundaries between  $\gamma = \alpha + \frac{1}{2}i$  and  $\gamma = \beta i$

$$\gamma = \frac{1}{2}i$$

On stability boundaries  $\alpha = \frac{1}{2}\kappa$ , so that

$$\gamma = \frac{1}{2}\kappa$$

or

$$\gamma = \frac{1}{2}\kappa + \frac{1}{2}i$$

Except for the calculations leading to figure 8,  $E_1 = 0$ . In any case  $E_1$  was taken as a known quantity. Then, depending on the part of the curve being calculated, either  $\kappa$  was fixed and corresponding values of  $E$  were sought, or vice versa.

On periodicity boundaries where  $\gamma = 0$ , equations A-20, A-21, and A-22 are

$$r_n = \frac{1}{\frac{2}{E}(n^2 + \frac{1}{4}\kappa^2 - E_1) - r_{n+1}}$$



$$\bar{r}_n = \frac{1}{\frac{2}{E}(n^2 + \frac{1}{4}\kappa^2 - E_1) - \bar{r}_{n+1}} \quad (\text{A-23})$$

$$r + \bar{r} = \frac{2}{E}(\frac{1}{4}\kappa^2 - E_1)$$

It is evident that  $r_n$  and  $\bar{r}_n$  are real and

$$r_n = \bar{r}_n$$

so that equation A-23 is

$$r_1 = \frac{1}{E}(\frac{1}{4}\kappa^2 - E_1)$$

On periodicity boundaries where  $\gamma = \frac{1}{2}i$

$$r_n = \frac{1}{\frac{2}{E}[(n+\frac{1}{2})^2 + \frac{1}{4}\kappa^2 - E_1] - r_{n+1}}$$

$$\bar{r}_n = \frac{1}{\frac{2}{E}[(n-\frac{1}{2})^2 + \frac{1}{4}\kappa^2 - E_1] - \bar{r}_{n+1}}$$

$$\bar{r}_n = r_{n-1}$$

and equation A-23 is

$$r_0 + r_1 = \frac{2}{E}(\frac{1}{4}\kappa^2 + \frac{1}{4} - E_1)$$

On stability boundaries where  $\gamma = \frac{1}{2}\kappa$ ,

$$r_n = \frac{1}{\frac{2}{E}(n^2 - E_1 - in\kappa) - r_{n+1}}$$

$$\bar{r}_n = \frac{1}{\frac{2}{E}(n^2 - E_1 + in\kappa) - r_{n+1}}$$

$$\bar{r}_n = r_n^*$$

and

$$R(r_1) = \frac{E_1}{E}$$

On stability boundaries where  $\gamma = \frac{1}{2}\kappa + \frac{1}{2}i$ ,

$$r_n = \frac{1}{\frac{2}{E}[(n+\frac{1}{2})^2 - E_1 - i(n+\frac{1}{2})\kappa] - r_{n+1}}$$

$$\bar{r}_n = \frac{1}{\frac{2}{E}[(n-\frac{1}{2})^2 - E_1 - i(n-\frac{1}{2})\kappa] - \bar{r}_{n+1}}$$

$$\bar{r}_n = r_{n-1}^*$$

$$r_1 + r_0^* = \frac{2}{E}(\frac{1}{4} - E_1 - \frac{1}{4}\kappa i)$$

On lines of constant  $\nu$  where  $\gamma = \nu + \frac{1}{2}\kappa$ ,

$$r_n = \frac{1}{\frac{2}{E}[n^2 - \nu(\nu + \kappa) - E_1 - in(2\nu + \kappa)] - r_{n+1}}$$

$$\bar{r}_n = \frac{1}{\frac{2}{E}[n^2 - \nu(\nu + \kappa) - E_1 + in(2\nu + \kappa)] - \bar{r}_{n+1}}$$

$$\bar{r}_n = r_n^*$$

$$R(r_1) = -\frac{1}{E}[\nu(\nu + \kappa) + E_1]$$

On lines of constant  $\nu$  where  $\gamma = \nu + \frac{1}{2}\kappa + \frac{1}{2}i$ ,

$$r_n = \frac{1}{\frac{2}{E}[(n + \frac{1}{2})^2 - \nu(\nu + \kappa) - E_1 - i(n + \frac{1}{2})(2\nu + \kappa)] - r_{n+1}}$$

$$\bar{r}_n = \frac{1}{\frac{2}{E}[(n - \frac{1}{2})^2 - \nu(\nu + \kappa) - E_1 + i(n - \frac{1}{2})(2\nu + \kappa)] - \bar{r}_{n+1}}$$

$$\bar{r}_n = r_{n-1}^* \quad (\text{A-24})$$

$$r_1 + r_0^* = \frac{2}{E}[\frac{1}{4} - \nu(\kappa + \nu) - (\nu + \frac{1}{2}\kappa)i] \quad (\text{A-25})$$

For each of these cases the scheme of calculation was as follows:

1. The value of  $E_1$  was fixed, usually at  $E_1 = 0$ .
2. For the case of lines of constant  $\nu$ , the value of  $\nu$  was fixed.
3. The value of  $\kappa$  (or in some cases the value of  $E$ ) was fixed.
4. Using a guessed value of  $E$  (or  $\kappa$ ),  $r_1$  and, if necessary,  $r_0$  were computed by repeated application of equation A-20, starting from some sufficiently high value of  $n$ . Note that equation A-21 is not used in the computation, being required only to establish the relation  $r_n = \bar{r}_n$ .
5. The difference between the two sides of equation A-25 was determined.
6. A new guess at  $E$  (or  $\kappa$ ) was made, usually by interpolation.
7. When a value of  $E$  (or  $\kappa$ ) was found for which equation A-25 was sufficiently nearly satisfied, a new  $\kappa$  (or  $E$ ) was fixed and steps 4 through 6 repeated.

The curves shown in figure 12 were calculated by writing the Taylor expansion for  $\xi$  and  $\xi'$  from equation 11.

$$\zeta'' = -(\kappa + \kappa_1 u)\zeta' - (E \cos \tau + E_1)\zeta - h$$

$$\zeta''' = -(\kappa + \kappa_1 u)\zeta'' - (\kappa_1 u' + E \cos \tau + E_1)\zeta' + E\zeta \sin \tau$$

$$\zeta(\tau + \overline{\Delta\tau}) = \zeta(\tau) + \overline{\Delta\tau}\zeta'(\tau) + \frac{1}{2}\overline{\Delta\tau}^2\zeta''(\tau) + \frac{1}{6}\overline{\Delta\tau}^3\zeta'''(\tau)$$

$$\zeta'(\tau + \overline{\Delta\tau}) = \zeta'(\tau) + \overline{\Delta\tau}\zeta''(\tau) + \frac{1}{2}\overline{\Delta\tau}^2\zeta'''(\tau)$$

where  $\overline{\Delta\tau}$  is the amount by which  $\tau$  is incremented, usually  $\pi/125$  (that is,  $\frac{1}{250}$  cycle of  $\cos \tau$ ), and  $u$  is the magnitude of the velocity as represented by  $|\zeta'|$ . In these computations  $u$  was taken as  $|\zeta'|$  and the contribution of the horizontal component of the velocity was ignored, even though where the horizontal unstable region overlaps the vertical stable region, the horizontal contribution is not negligible. Most of the region in  $\kappa$ - $E$  space where there is instability in both directions has been hitherto inaccessible to experimental observation in any case. Near the nose of the first instability curve where observation in the first unstable region is easy, the horizontal contribution damps out.

Computations were carried out on Mathetron calculators and on a Univac 1108 computer.

## APPENDIX B

### LIST OF SYMBOLS

$A$	integration constant in solution to dimensionless equation of motion
$A_n$	coefficients in expression for potential $\Phi$ in cylindrical coordinates
$\bar{A}_n$	coefficients in expression for potential $\Phi$ in spherical coordinates
$\bar{a}$	coefficient in Mathieu's equation
$a_n$	coefficients of Fourier expansion of $p(\tau)$ in terms of $e^{in\tau}$
$B$	integration constant in solution to dimensionless equation of motion
$C$	ratio of gradient of vertical component of electric field at null point to potential difference between electrodes
$c$	constant given by $\omega^2  a_0 d  / g$
$C_{\pm}$	constants used to define electrode hyperboloids
$C_{dc}$	ratio of field strength at center of chamber to potential difference between sheets of hyperboloid
$C_n$	coefficients of Fourier expansion of $p(\tau)$ in terms of $\cos(n\tau \pm \phi_n)$
$d$	diameter of particle
$E$	peak value of field strength due to alternating potential difference between electrodes
$E_1$	field strength due to constant potential difference between electrodes
$E_c$	$E_1 + E \cos \omega t$
$E_{dc}$	field strength due to potential difference between sheets of two-sheet electrodes
$e$	2.718281828 . . .
$E$	coefficient of $\zeta \cos \omega t$ in dimensionless equation of motion (due to $E$ )
$E_1$	coefficient of $\zeta$ in dimensionless equation of motion (due to $E_1$ )
$g$	acceleration due to gravity
$g$	magnitude of $g$
$h$	constant term in dimensionless equation of motion (due to gravity and $E_{dc}$ )
$i$	$\sqrt{-1}$



$I_1$	first region where $\gamma = \beta i$
$I_n$	imaginary part of $a_n$
$K_D$	coefficient describing aerodynamic drag
$\hat{k}$	unit vector along vertical axis (z axis)
$m$	mass of particle
$n$	summation index
$P_n$	$n$ th Legendre polynomial
$P$	periodic factor in solution to equation of motion
$p$	periodic solution to inhomogeneous equation
$q$	charge on particle
$\bar{q}$	coefficient in Mathieu's equation
$\mathbf{R}$	position of particle
$R(X)$	real part of $X$
$R_n$	real part of $a_n$
$\text{Re}$	Reynolds number
$R_0$	lowest $\gamma = \alpha$ region
$R_n S$	stable part of $\gamma = \alpha$ or $\gamma = \alpha - \frac{1}{2}i$ region
$R_n U$	unstable part of $\gamma = \alpha$ or $\gamma = \alpha + \frac{1}{2}i$ region
$r$	radial coordinate in cylindrical coordinate system
$r_s$	radial coordinate in spherical coordinate system
$r_0$	inner radius of one-sheet hyperboloidal electrode
$\hat{r}_0$	unit radial vector in cylindrical coordinate system
$t$	time
$u$	magnitude of particle velocity divided by particle diameter
$V$	peak value of alternating part of potential difference between electrodes
$V_1$	constant part of potential difference between electrodes
$V_{dc}$	potential difference between sheets of two-sheet electrode

$x, y$	horizontal cartesian coordinates
$z$	vertical cartesian or cylindrical coordinate
$z_0$	half-height of hyperboloidal chamber (distance from null point to nose of two-sheet hyperboloidal electrode)
$\alpha$	real part of $\gamma$ for equation of motion
$\bar{\alpha}$	real part of $\bar{\gamma}$ for Mathieu's equation
$\beta$	imaginary part of $\gamma$ for equation of motion
$\bar{\beta}$	imaginary part of $\gamma$ for Mathieu's equation
$\gamma$	exponential coefficient in solution to equation of motion
$\bar{\gamma}$	exponential coefficient in solution to Mathieu's equation
$\xi$	solution to dimensionless equation of motion
$\xi_1, \xi_2$	two independent solutions to dimensionless equation of motion for vertical motion
$\bar{\xi}, \bar{\xi}_1, \bar{\xi}_2$	solutions to Mathieu's equation
$\eta$	viscosity of air
$\theta$	equatorial angle in cylindrical coordinate system
$\theta_s$	polar angle in spherical coordinate system
$\kappa$	drag term coefficient in dimensionless equation of motion
$\kappa_1$	velocity squared drag term coefficient in dimensionless equation of motion
$\nu$	$\alpha - \frac{1}{2}\kappa$
$\xi, \xi_1, \xi_2$	solutions to dimensionless equations of motion for horizontal motion
$\pi$	3.14159265 . . .
$\rho$	density of air
$\rho_s$	density of particle material
$\tau$	$\omega t$ (independent variable in dimensionless equation of motion)
$\bar{\tau}$	independent variable in Mathieu's equation
$\tau_0$	value of $\tau$ at coincidence point
$\Phi$	potential function

$\Phi_n$	lag angle for $n$ th term of series representing $p(\tau)$ in terms of cosines
$\psi_n$	$n\phi_1 - \phi_n$
$\sigma$	surface tension of particle material
$\omega$	angular frequency of alternating potential difference between electrodes
asterisks	complex conjugate
dots	differentiation with respect to time ( $t$ )
primes	differentiation with respect to $\tau$

# DISTRIBUTION LIST 3

Names	Copies	Names	Copies
CHEMICAL SYSTEMS LABORATORY		DEPARTMENT OF THE ARMY	
SAFETY OFFICE		HQDA (DAMO-SSC)	1
Attn: DRDAR-CLF	1	WASH DC 20310	
PLANS & PROGRAMS OFFICE		CINCUSAREUR	
Attn: DRDAR-CLR-L	4	Attn: AEAGC-RSI	1
AUTHOR'S COPIES: Research Division	3	APO New York 09403	
BIOMEDICAL LABORATORY		Deputy Chief of Staff for Research,	
Attn: DRDAR-CLL-B	1	Development & Acquisition	
Attn: DRDAR-CLL-M	1	Attn: DAMA-CSM-CM	1
Attn: DRDAR-CLL-MC	1	Attn: DAMA-ARZ-D	1
Attn: DRDAR-CLL-V	1	Washington, DC 20310	
CB DETECTION & ALARMS DIVISION		US Army Research and Standardization	
Attn: DRDAR-CLC-C	1	Group (Europe)	1
Attn: DRDAR-CLC-E	1	Attn: Chief, Chemistry Branch	
DEVELOPMENTAL SUPPORT DIVISION		Box 65, FPO New York 09510	
Attn: DRDAR-CLJ-R	3	HQDA (DAMI-FIT)	1
Attn: DRDAR-CLJ-L	3	WASH, DC 20310	
Attn: DRDAR-CLJ-M	1	Commander	
ENVIRONMENTAL TECHNOLOGY DIVISION		HQ US Army Medical Command, Europe	
Attn: DRDAR-CLT-D	3	Attn: AEMPM	1
MUNITIONS DIVISION		APO New York 09403	
Attn: DRDAR-CLN	5	US ARMY HEALTH SERVICE COMMAND	
PHYSICAL PROTECTION DIVISION		Superintendent	
Attn: DRDAR-CLW-C	1	Academy of Health Sciences	
Attn: DRDAR-CLW-P	1	US Army	
RESEARCH DIVISION		Attn: HSA-CDC	1
Attn: DRDAR-CLB	1	Attn: HSA-IHE	1
Attn: DRDAR-CLB-B	1	Fort Sam Houston, TX 78234	
Attn: DRDAR-CLB-C	1	US ARMY MATERIEL DEVELOPMENT AND	
Attn: DRDAR-CLB-P	1	READINESS COMMAND	
Attn: DRDAR-CLB-R	1	Commander	
Attn: DRDAR-CLB-T	1	US Army Materiel Development and Readiness Command	
Attn: DRDAR-CLB-TE	1	Attn: DRCLDC	1
SYSTEMS ASSESSMENTS OFFICE		Attn: DRCSF-P	1
Attn: DRDAR-CLY-A	1	5001 Eisenhower Ave	
Attn: DRDAR-CLY-R	1	Alexandria, VA 22333	
DEPARTMENT OF DEFENSE		Office of the Project Manager for Chemical Demilitarization	
Administrator		and Installation Restoration	
Defense Documentation Center		Attn: DRCPM-DR-T	2
Attn: Accessions Division (DDC-TC)	12	Aberdeen Proving Ground, MD 21010	
Cameron Station		Human Engineering Laboratory HFE Detachment	
Alexandria, VA 22314		Attn: DRXHE-EA	1
Director		Building E3220	
Defense Intelligence Agency		APG-Edgewood Area	
Attn: DB-4G1	1	Commander	
Washington, DC 20301		US Army Foreign Science & Technology Center	
		Attn: DRXST-CX2	1
		220 Seventh St., NE	
		Charlottesville, VA 22901	



# DISTRIBUTION LIST 3 (Contd)

Names	Copies	Names	Copies
Commander US Army Missile Research and Development Command Redstone Scientific Information Center Attn: DRDMI-TBD Redstone Arsenal, AL 35809	1	Commander Rocky Mountain Arsenal Attn: SARRM-QA Attn: SARRM-MD Commerce City, CO 80022	1 1
Director DARCOM Field Safety Activity Attn: DRXOS-C Charlestown, IN 47111	1	Commander Pine Bluff Arsenal Attn: SARPB-ETA Pine Bluff, AR 71611	1
Commander US Army Materiel Development and Readiness Command Installations and Services Activity Attn: DRCIS-RI-IU Rock Island, IL 61299	1	US ARMY TRAINING & DOCTRINE COMMAND  Commandant US Army Infantry School Attn: NBC Division Fort Benning, GA 31905	1
US ARMY ARMAMENT RESEARCH AND DEVELOPMENT COMMAND  Commander US Army Armament Research and Development Command Attn: DRDAR-LCE-M Attn: DRDAR-LCH Attn: DRDAR-LCU Attn: DRDAR-SER Attn: DRDAR-TSS Dover, NJ 07801	 1 1 1 1 2	Commandant US Army Missile & Munitions Center & School Attn: ATSK-CD-MD Attn: ATSK-DT-MU-EOD Redstone Arsenal, AL 35809	 1 1
Director Ballistic Research Laboratory Attn: DRDAR-TSB-S Building 328 Aberdeen Proving Ground, MD 21005	1	Commandant US Army Military Police School/Training Center Attn: ATZN-CDM Attn: ATZN-TDP-C Fort McClellan, AL 36205	1 1
CDR, APG USA ARRADCOM Attn: DRDAR-GCL Aberdeen Proving Ground, MD 21010	1	Commander US Army Infantry Center Attn: ATSH-CD-MS-C Fort Benning, GA 31905	1
US ARMY ARMAMENT MATERIEL READINESS COMMAND		Commandant US Army Ordnance & Chemical Center & School Attn: ATSL-CL-CD Aberdeen Proving Ground, MD 21005	1
Commander US Army Armament Materiel Readiness Command Attn: DRSAR-ASN Attn: DRSAR-IMB-C Attn: DRSAR-SF Rock Island, IL 61299	1 1 1	US ARMY TEST & EVALUATION COMMAND  Commander US Army Test & Evaluation Command Attn: DRSTE-FA Aberdeen Proving Ground, MD 21005	1
CDR, APG USA ARRCOM Attn: SARTE Aberdeen Proving Ground, MD 21010	1	Commander US Army Cold Regions Test Center Attn: STECR-TD APO Seattle, WA 98733	1
Commander US Army Dugway Proving Ground Attn: Technical Library, Docu Sect Dugway, UT 84022	1	DEPARTMENT OF THE NAVY  Chief of Naval Research Attn: Code 443 800 N. Quincy Street Arlington, VA 22217	1



# DISTRIBUTION LIST 3 (Contd)

Names	Copies	Names	Copies
Commander Naval Explosive Ordnance Disposal Facility Attn: Army Chemical Officer, Code 604 Indianhead, MD 20640	1	HQ AFISC/SEV Norton AFB, CA 92409	1
Commander Naval Surface Weapons Center White Oak Laboratory Attn: Tech Lib & Info Svcs Br Silver Spring, MD 20910	1	NORAD Combat Operations Center/DBN Cheyenne Mtn Complex, CO 80914	1
Commander Nuclear Weapons Training Group, Atlantic Naval Air Station Attn: Code 21 Norfolk, VA 23511	1	OUTSIDE AGENCIES	
Chief, Bureau of Medicine & Surgery Department of the Navy Washington, DC 20372	1	Battelle, Columbus Laboratories Attn: TACTEC 505 King Avenue Columbus, OH 43201	1
Commander Naval Weapons Center Attn: A. B. Galloway/Code 3171 Attn: Technical Library/Code 233 China Lake, CA 93555	1	Director of Toxicology National Research Council 2101 Constitution Ave, NW Washington, DC 20418	1
US MARINE CORPS		ADDITIONAL ADDRESSEES	
Director, Development Center Marine Corps Development & Education Command Attn: Fire Power Division Quantico, VA 22134	1	US Public Health Service Room 17A-46 (CPT Osheroff) 5600 Fishers Lane Rockville, MD 20857	1
DEPARTMENT OF THE AIR FORCE		Commander US Army Environmental Hygiene Agency Attn: Librarian, Bldg 2100 Aberdeen Proving Ground, MD 21010	1
HQ Foreign Technology Division (AFSC) Attn: PDRR Wright-Patterson AFB, OH 45433	1	Commander DARCOM, STITEUR Attn: DRXST-ST1 Box 48, APO New York 09710	1
Commander Aeronautical Systems Division Attn: ASD/AELD Wright-Patterson AFB, OH 45433	1	Commander US Army Science & Technology Center-Far East Office APO San Francisco 96328	1
AMRL/MEB Wright-Patterson AFB, OH 45433	1	HQDA DASG-RDZ (SGRD-PL) WASH DC 20314	1
HQ, USAF/SGPR Forrestal Bldg WASH DC 20314	1	Commander USEUCOM Attn: ECJ5-O/LTC James H. Alley APO New York 09128	1
HO USAF/RDPN WASH DC 20330	1		